



LAWRENCE
LIVERMORE
NATIONAL
LABORATORY

LLNL-JRNL-440311

The dynamical core, physical parameterizations, and basic simulation characteristics of the atmospheric component of the GFDL global coupled model CM3

L. J. Donner, B. L. Wyman, R. S. Hemler, L. W. Horowitz, Y. Ming, M. Zhao, J. C. Golaz, P. Ginoux, S. J. Lin, M. D. Schwarzkopf, J. Austin, G. Alaka, W. F. Cooke, T. L. Delworth, S. M. Freidenreich, C. T. Gordon, S. Griffies, I. M. Held, W. J. Hurlin, S. A. Klein, T. R. Knutson, A. R. Langenhorst, H. C. Lee, Y. Lin, B. I. Magi, S. L. Malyshev, P. C. D. Milly, V. Naik, M. J. Nath, R. Pincus, J. J. Ploshay, V. Ramaswamy, C. J. Seman, E. Shevliakova, J. J. Sirutis, W. F. Stern, R. J. Stouffer, R. J. Wilson, M. Winton, A. T. Wittenberg, F. Zeng

July 7, 2010

Journal of Climate

Disclaimer

This document was prepared as an account of work sponsored by an agency of the United States government. Neither the United States government nor Lawrence Livermore National Security, LLC, nor any of their employees makes any warranty, expressed or implied, or assumes any legal liability or responsibility for the accuracy, completeness, or usefulness of any information, apparatus, product, or process disclosed, or represents that its use would not infringe privately owned rights. Reference herein to any specific commercial product, process, or service by trade name, trademark, manufacturer, or otherwise does not necessarily constitute or imply its endorsement, recommendation, or favoring by the United States government or Lawrence Livermore National Security, LLC. The views and opinions of authors expressed herein do not necessarily state or reflect those of the United States government or Lawrence Livermore National Security, LLC, and shall not be used for advertising or product endorsement purposes.

**The Dynamical Core, Physical Parameterizations, and
Basic Simulation Characteristics of the Atmospheric
Component of the GFDL Global Coupled Model CM3**

Leo J. Donner, Bruce L. Wyman, Richard S. Hemler, Larry W. Horowitz, NOAA/GFDL, Princeton, New Jersey; Yi Ming, Ming Zhao, UCAR/GFDL, Princeton, New Jersey; Jean-Christophe Golaz, Paul Ginoux, S.-J. Lin, M. Daniel Schwarzkopf, NOAA/GFDL, Princeton, New Jersey; John Austin, UCAR/GFDL, Princeton, New Jersey; Ghassan Alaka, Colorado State University, Fort Collins, Colorado; William F. Cooke, High Performance Technologies, Inc./GFDL, Princeton, New Jersey; Thomas L. Delworth, Stuart M. Freidenreich, C.T. Gordon, Stephen Griffies, Isaac M. Held, William J. Hurlin, NOAA/GFDL, Princeton, New Jersey; Stephen A. Klein, Program for Climate Model Diagnosis and Intercomparison, Lawrence Livermore National Laboratory, Livermore, California; Thomas R. Knutson, NOAA/GFDL, Princeton, New Jersey; Amy R. Langenhorst, Hyun-Chul Lee, High Performance Technologies, Inc./GFDL, Princeton, New Jersey; Yanluan Lin, UCAR/GFDL, Princeton, New Jersey; Brian I. Magi, Sergey L. Malyshev, Princeton University/GFDL, Princeton, New Jersey; P.C.D. Milly, U.S. Geological Survey, Princeton, New Jersey; Vaishali Naik, High Performance Technologies, Inc./GFDL, Princeton, New Jersey; Mary J. Nath, NOAA/GFDL, Princeton, New Jersey; Robert Pincus, University of Colorado/ESRL, Boulder, Colorado; Jeffrey J. Ploshay, V. Ramaswamy, Charles J. Seman, NOAA/GFDL, Princeton, New Jersey; Elena Shevliakova, Princeton University/GFDL, Princeton, New Jersey; Joseph J. Sirutis, William F. Stern, Ronald J. Stouffer, R. John Wilson, Michael Winton, Andrew T. Wittenberg, and Fanrong Zeng, NOAA/GFDL, Princeton, New Jersey

24 June 2010

For submission to *Journal of Climate*

Corresponding Author Address: Leo J. Donner, Geophysical Fluid Dynamics Laboratory/NOAA, Princeton University Forrestal Campus, 201 Forrestal Rd., Princeton, New Jersey 08540, leo.j.donner@noaa.gov

ABSTRACT

1 The Geophysical Fluid Dynamics Laboratory (GFDL) has developed a
2 coupled general circulation model (CM3) for atmosphere, oceans, land, and
3 sea ice. The goal of CM3 is to address emerging issues in climate change,
4 including aerosol-cloud interactions, chemistry-climate interactions, and cou-
5 pling between the troposphere and stratosphere. The model is also designed
6 to serve as the physical-system component of earth-system models and mod-
7 els for decadal prediction in the near-term future, for example, through im-
8 proved simulations in tropical land precipitation relative to earlier-generation
9 GFDL models. This paper describes the dynamical core, physical parameter-
10 izations, and basic simulation characteristics of the atmospheric component
11 (AM3) of this model.

12 Relative to GFDL AM2, AM3 includes new treatments of deep and shal-
13 low cumulus convection, cloud-droplet activation by aerosols, sub-grid vari-
14 ability of stratiform vertical velocities for droplet activation, and atmospheric
15 chemistry driven by emissions with advective, convective, and turbulent
16 transport. AM3 employs a cubed-sphere implementation of a finite-volume
17 dynamical core and is coupled to LM3, a new land model with eco-system
18 dynamics and hydrology.

19 Most basic circulation features in AM3 are simulated as realistically, or
20 more so, than in AM2. In particular, dry biases have been reduced over South
21 America. In coupled mode, the simulation of Arctic sea ice concentration
22 has improved. AM3 aerosol optical depths, scattering properties, and surface

23 clear-sky downward shortwave radiation are more realistic than in AM2. The
24 simulation of marine stratocumulus decks and the intensity distributions of
25 precipitation remain problematic, as in AM2.

26 The last two decades of the 20th century warm in CM3 by $.40^{\circ}\text{C}$ relative
27 to 1881-1920. The Climate Research Unit (CRU) analysis of observations
28 show warming of $.56^{\circ}\text{C}$ over this period. Although CM3 includes anthro-
29 pogenic cooling by aerosol-cloud interactions, its warming by late 20th cen-
30 tury is only slightly less realistic than in CM2.1, which warmed $.66^{\circ}\text{C}$ and did
31 not include aerosol-cloud interactions. The improved simulation of the di-
32 rect aerosol effect (apparent in surface clear-sky downward radiation) in CM3
33 evidently acts in concert with its simulation of cloud-aerosol interactions to
34 limit greenhouse gas warming in a way that is consistent with observed global
35 temperature changes.

36 1. Introduction

37 The study of climate and climate change using general circulation mod-
38 els (GCMs) continues to advance rapidly, with impetus from widespread
39 societal concern about anthropogenic and natural climate change, unprece-
40 dented global and field observational programs, and advances in theoretical
41 and process-level understanding of atmospheric, oceanic, cryospheric, and
42 terrestrial processes. The purpose of this paper is to describe recent de-
43 velopment in the atmospheric component (AM3) of the Geophysical Fluid
44 Dynamics Laboratory (GFDL) coupled model (CM3). AM3 is built upon
45 the scientific and software framework of GFDL AM2 (Geophysical Fluid Dy-
46 namics Laboratory Global Atmospheric Model Development Team [GFDL
47 GAMDT], 2004). Its major developmental thrusts were chosen to enable
48 AM3 to address several key, emerging questions in climate and climate change
49 that could not be addressed with AM2: (1) What are the roles of aerosol-
50 cloud interactions, specifically, indirect effects of aerosols? (2) What are the
51 dominant chemistry-climate interactions? AM3 development also aimed at
52 enhanced capabilities for addressing emerging questions when coupled with
53 bio-geochemical and ocean models: (1) What is the inter-play between cli-
54 mate and key bio-geochemical cycles? (2) To what extent is decadal pre-
55 diction possible? The model also includes advances in the dynamical core,
56 radiation, and other components.

57 Addressing these scientific questions implied particular approaches to
58 AM3 development. In order to model aerosol-cloud interactions using a

59 physically based treatment of aerosol activation, parameterizations for sub-
60 grid variability of vertical velocity are important. This is because aerosol
61 activation depends strongly on *local* vertical velocity, which, for both strati-
62 form and convective clouds, can depart strongly from the large-scale average.
63 AM3 parameterizes sub-grid vertical velocities for all clouds. In order to
64 study chemistry-climate interactions, AM3 specifies chemical emissions and
65 includes large-scale and convective transport, wet and dry removal, and key
66 tropospheric and stratospheric reactions. AM3's stratospheric resolution has
67 been increased, and its upper boundary has been raised, to treat stratospheric
68 processes more comprehensively. AM3 itself does not include carbon, nitro-
69 gen, or other bio-geochemical cycles, but particular attention has been given
70 to improving its simulation of tropical precipitation, in order to enhance its
71 usefulness as a component of earth-system models. AM3's improved strato-
72 spheric resolution is also necessary for future research on phenomena such as
73 the Southern Hemisphere Annular Mode, which likely plays a role in interan-
74 nual variability important for decadal prediction (Thompson and Solomon,
75 2006).

76 Section 2 describes AM3's dynamical core. Section 3 presents its physical
77 parameterizations, while Appendix 1 presents brief summaries of the land,
78 ocean, and sea-ice models used with AM3 in CM3. Section 4 illustrates
79 basic simulation characteristics of AM3 with prescribed sea surface temper-
80 atures and in coupled mode. The inclusion of aerosol-cloud interactions in
81 AM3 links cloud radiative properties to anthropogenic aerosols, whose op-

82 tical properties and direct effects on shortwave radiation agree better with
83 observations than in AM2. Section 4 shows that the overall impact of an-
84 thropogenic changes in trace gases and aerosols is consistent with observed
85 global surface temperature changes.

86 **2. Dynamical Core**

87 As in CM2.1 (Delworth et al. 2006), the dynamical core used in AM3/CM3
88 follows the finite-volume algorithms described in Lin and Rood (1996, 1997)
89 and Lin (1997, 2004), with the following major modifications.

90 In an effort to enhance the model’s parallel computing efficiency and
91 to improve simulation quality in polar regions, the dynamical core formu-
92 lated on, and optimized specifically for, the latitude-longitude grid has been
93 significantly modified to use a general curvilinear coordinate system. The
94 non-orthogonal gnomonic projection in the general cubed-sphere geometry
95 described by Putman and Lin (2007) is chosen due to its excellent grid unifor-
96 mity and better overall accuracy. The use of the non-orthogonal coordinate
97 system necessitated major changes to the transport operators (Putman and
98 Lin, 2007) and the need to compute both the co- and contra-variant wind
99 components (e.g., Sadourny, 1972).

100 Compared to the original latitude-longitude grid formulation, the use of
101 the cubed-sphere grid in the new finite-volume core greatly improved the
102 computational efficiency due to two major algorithmic modifications. First,
103 the flux-form semi-Lagrangian extension (Lin and Rood, 1996) needed to

104 stabilize the (large-time-step) transport processes near the poles is no longer
105 needed with the use of the cubed-sphere grid. Second, and related to the first,
106 the polar Fourier filtering required for the stabilization of the fast waves is also
107 no longer needed. Both modifications led to greatly improved computation
108 and communication load balancing, enabling the efficient use of 2D domain
109 decomposition on each of the six faces of the cube.

110 The model's horizontal resolution is denoted as Cn, where n is an integer
111 number indicating total number of cells (finite volumes) along each edge of
112 the cube. In AM3, the model's resolution is C48. The total number of
113 cells on the sphere is therefore $6 \times 48 \times 48 = 13,824$, and the size of the grid cell
114 varies from 163 km (at the 6 corners of the cubed sphere) to 231 km (near
115 the center of each face). The C48 resolution model scales roughly an order
116 of magnitude better (can use 864, versus 30, central processing units) than
117 its latitude-longitude counterpart (2x2.5 degrees resolution) used in CM2.1,
118 enabling nearly the full use of GFDL 1024-core SGI Altix-3000 system.

119 The vertical co-ordinate in AM3 follows Simmons and Burridge (1981),
120 but the number of layers has been increased to 48 (from 24 layers in AM2).
121 The uppermost level in AM3 has a pressure of 1 Pa, a height of about 86
122 km for a surface pressure of 1013.25 hPa and scale height of 7.5 km (equiva-
123 lently, isothermal with a temperature of approximately 256.2 K), compared
124 to around 35 km in AM2. The augmentation in vertical levels is aimed at
125 resolving the stratosphere sufficiently well that its basic chemical and dy-
126 namical processes can be reasonably simulated. Table 1 shows the positions

127 of the intermediate levels, which bound AM3's layers.

128 **3. Physical Parameterizations**

129 *a. Radiation*

130 The basic shortwave and longwave radiation algorithms are described
131 in Freidenreich and Ramaswamy (1999) and Schwarzkopf and Ramaswamy
132 (1999), respectively, modified as in GFDL GAMDT (2004). The solar con-
133 stant is from the Total Irradiance Monitor (Kopp et al., 2005), as recom-
134 mended for Climate Model Intercomparison 5 ([http://www.geo.fu-berlin.de/](http://www.geo.fu-berlin.de/en/met/ag/strat/forschung/SOLARIS/Input_data/CMIP5_solar_irradiance.html)
135 [en/met/ag/strat/forschung/SOLARIS/Input_data/CMIP5_solar_irradiance.html](http://www.geo.fu-berlin.de/en/met/ag/strat/forschung/SOLARIS/Input_data/CMIP5_solar_irradiance.html)).

136 1) SUB-GRID VARIABILITY AND OVERLAP

137 All-sky radiative transfer calculations account for the effect of clouds us-
138 ing the Monte Carlo Independent Column Approximation (Pincus et al.,
139 2003), which treats variability by creating a set of sub-columns consistent
140 with cloud properties (including variability) and vertical structure (i.e., over-
141 lap). The in-cloud distribution of ice and water content in stratiform clouds
142 is diagnosed from the cloud fraction and condensate amount (Pincus et al.,
143 2006), and vertical structure assumes that the rank correlation of total water
144 falls off exponentially with the distance between layers using a scale height
145 of 1 km (Pincus et al., 2005). These formulations differ from those in AM2
146 and allow cloud optical properties to be used as predicted, rather than being
147 arbitrary multiplied by 0.85 as in AM2. The radiative properties of shallow

148 and deep convective clouds (Section 3e) are also included. Convective clouds
149 are assumed to be internally homogeneous and to obey maximum overlap.
150 When convective clouds occur in a sub-column they replace any stratiform
151 clouds in layers where both clouds occur, which slightly decreases the overall
152 stratiform cloud amount.

153 Effective radius in each sub-column is computed assuming that the pre-
154 dicted cloud drop number is uniform for each cloud type within each large-
155 scale column. In stratiform clouds and shallow cumulus, drop size depends
156 on aerosol activation, as described in Section 3f.

157 2) CLOUD OPTICS

158 The sizes of cloud droplets in stratiform and shallow cumulus clouds de-
159 pend on aerosol activation and are determined using the procedures described
160 in Section 3f. In deep cumulus updraft cells, the sizes of liquid droplets follow
161 Bower et al. (1994). Size-dependent shortwave optical properties for cloud
162 liquid follow Slingo (1989). Longwave liquid optical properties follow Held et
163 al. (1993) and depend on water path but not particle size. AM3 does not link
164 ice nucleation to crystal sizes. In shallow cumulus and stratiform ice clouds,
165 ice particle sizes are diagnosed as a function of temperature, based on aircraft
166 observations (Donner et al., 1997) with radiative properties following Fu and
167 Liou (1993). In mesoscale updrafts associated with deep convection, ice crys-
168 tals increase in size with distance from the top of updraft as in McFarquhar
169 et al. (1999), except that McFarquhar et al.'s (1999) heights are replaced

170 with equivalent normalized fractional distances between the top and base of
171 the mesoscale updraft. Ice crystals in cumulus cell updrafts are assigned a
172 generalized effective size of $18.6 \mu\text{m}$, a value noted by Fu (1996) from the
173 early temporal evolution (most likely dominated by deep cells) of a convec-
174 tive system in the Central Equatorial Pacific Experiment. Solar and infrared
175 radiative properties of ice crystals in cell updrafts and mesoscale anvils are
176 obtained from Fu (1996) and Fu et al. (1998), respectively.

177 3) GAS CONCENTRATIONS

178 Historical concentrations of carbon dioxide, nitrous oxide, methane and
179 halocarbons (CFC-11, CFC-12, CFC-113, and HCFC-22) are obtained from
180 www.iiasa.ac.at/web-apps/tnt/RcpDb/, where the Representative Concen-
181 tration Pathways may also be found. Note that the methane specification
182 for radiation differs from the methane obtained from the chemistry calcu-
183 lations described in Section 3g. Tropospheric and stratospheric ozone are
184 modeled as described in Section 3g.

185 4) AEROSOL OPTICS

186 The effects of volcanoes are included in the AM3 and CM3 simulations
187 described in Section 4. Sulfur-dioxide emissions from volcanoes are described
188 in Section 3f. Direct injection of sulfur into the stratosphere from volcanic
189 eruptions is not included, nor is carbonyl-sulfide chemistry, a major source
190 of background stratospheric aerosol. To compensate, in the stratosphere, a
191 time series of volcanic optical properties is specified as in Stenchikov et al.

192 (2006).

193 Aerosol optical properties (i.e., extinction efficiency, single-scattering albedo
194 and asymmetry factor) are based on Mie theory, assuming all particles spher-
195 ical. Log-normal size distribution is assumed for sulfate and carbonaceous
196 aerosols. The geometric mean radius and standard deviation of the log-
197 normal distribution for sulfate and black carbon are from Haywood and Ra-
198 maswamy (1998), and for organics from Hess et al. (1998). The mass size
199 distribution of dust and sea-salt is assumed constant within five bins from 0.1
200 to 10 μm . Hygroscopic growth is considered for sulfate, sea-salt, and aged
201 (hydrophilic) organic carbon. We model the hygroscopic growth of sulfate
202 after that of pure ammonium sulfate (Tang and Munkelwitz, 1994), of sea-
203 salt as pure sodium chloride (Tang et al., 1997), and of hydrophilic organics
204 as a mixture of acids and insoluble organics (Ming et al., 2005). The refrac-
205 tive indices of sulfate and black carbon are from Haywood and Ramaswamy
206 (1998), of organics from Hess et al. (1998), sea salt from Tang et al. (1997),
207 and dust from Balkanski et al. (2007) assuming 2.7% content of hematite.
208 Internal mixture of sulfate and aged (hydrophilic) black carbon is calculated
209 by volume weighted average of their refractive index. All other aerosols are
210 assumed externally mixed.

211 *b. Gravity Wave Drag*

212 Orographic gravity wave drag is parameterized using Stern and Pierre-
213 humbert (1988), as described in GFDL GAMDT (2004). Non-orographic

214 gravity-wave drag is parameterized using Alexander and Dunkerton (1999),
 215 which treats vertical propagation of wave components of a spectrum of grav-
 216 ity waves with a range of phase speeds and horizontal waves, assuming that
 217 the momentum associated with each wave component is deposited locally at
 218 the level of linear wave breaking. There are uncertainties in the seasonal, lat-
 219 itudinal, and height dependencies of gravity-wave sources and sinks. Alexan-
 220 der and Rosenlof (2003) found that parameters related to the sources and
 221 sinks varied from the tropics to the extra-tropics. In the AM3 application of
 222 Alexander and Dunkerton (1999), the momentum source is represented by
 223 a broad spectrum of wave speeds (half-width of 40 m s^{-1}) with a resolution
 224 of 2 m s^{-1} and a single horizontal wavelength of 300 km. The amplitude of
 225 the momentum source is 0.005 Pa in the northern middle and high latitudes,
 226 0.004 Pa in the tropics, and 0.003 Pa in the southern middle and high lati-
 227 tudes, with smooth transitions around 30° N and S . The asymmetry in the
 228 northern and southern sources improves the simulation of stratospheric zonal
 229 winds and polar temperatures. The wave launch height decreases smoothly
 230 from 350 hPa at the equator to near the surface at the poles. Optimizing
 231 the input parameters was eased by limiting the influence of the orographic
 232 wave drag parameterization to below 30 hPa. The scheme yields a reason-
 233 able semi-annual oscillation. However, the vertical resolution employed here
 234 is not sufficiently fine to enable simulation of the quasi-biennial oscillation
 235 (Giorgetta et al., 2006).

236 *c. Turbulence and Planetary Boundary Layer*

237 Turbulence and planetary boundary layers (PBLs) in AM3 are treated as
 238 in AM2. Lock et al. (2000) is used for convective PBLs and stratocumulus
 239 layers. Louis (1979) is employed for other unstable layers. Stability functions
 240 with thresholds dependent on Richardson number are adopted for stable
 241 layers. Variations in vertical diffusion coefficients are damped. Full details
 242 can be found in GFDL GAMDT (2004).

243 *d. Stratiform Clouds*

244 Cloud fraction, liquid, and ice in AM3 are prognosed based on Tiedtke
 245 (1993), with modifications mostly as described in GFDL GAMDT (2004).
 246 Detrainment of cloud liquid, cloud ice, and cloud fraction are treated slightly
 247 differently than in GFDL GAMDT (2004) to be consistent with the Donner
 248 et al. (2001) deep and Bretherton et al. (2004) shallow cumulus parame-
 249 terizations in AM3. Denoting the mixing ratio of liquid or ice or the cloud
 250 fraction by X , its stratiform tendency due to deep convection is

$$gD_{meso}X_{meso} - g\frac{\partial(M_{deep}\overline{X})}{\partial p}. \quad (1)$$

251 Here, D_{meso} is the rate of change with pressure of the mass flux in the de-
 252 training layers of mesoscale updrafts in convective systems. The sum of
 253 upward mass fluxes in deep cells and mesoscale updrafts, reduced by the
 254 downward mass fluxes in mesoscale downdrafts, is M_{deep} , while g and p de-
 255 note the gravity constant and pressure, respectively. An overbar denotes a

256 large-scale average. Detrainment from deep convective cells in Donner et al.
 257 (2001) is directed to the mesoscale circulations, which are part of the cumu-
 258 lus parameterization. Thus, detrainment into the stratiform clouds is from
 259 the mesoscale updrafts only.

260 The corresponding stratiform tendency due to shallow cumulus is

$$gD_{shal}(X^* - \bar{X}) - gM_{shal}\frac{\partial \bar{X}}{\partial p}, \quad (2)$$

261 where X^* denotes a property within shallow cumulus.

262 Microphysical processes, except for activation of liquid cloud drops (de-
 263 scribed in Section 3f), follow Rotstayn (1997) and Rotstayn et al. (2000), as
 264 described in GFDL GAMDT (2004). The number of activated aerosols de-
 265 pends on aerosol mass, composition, and vertical velocity. To account for the
 266 effect of sub-grid variability, the vertical velocity is assumed to be normally
 267 distributed within each model grid box and the activation computed by inte-
 268 gration over this distribution following Ghan et al. (1997). The mean of the
 269 distribution is the velocity driving the stratiform condensation in the Tiedtke
 270 (1993) parameterization, and the variance is related to the turbulence mixing
 271 coefficients. A minimum variance of 0.7 m s^{-1} is imposed. The integration is
 272 performed numerically using a 64-point Gauss-Hermite quadrature.

273 Finally, several parameters in the Tiedtke (1993) parameterization have
 274 been altered from their GFDL GAMDT (2004) values. The critical droplet
 275 radius for autoconversion is $8.2 \text{ } \mu\text{m}$. The erosion constants when vertical
 276 diffusion is active, when convection (shallow, deep, or both) is active with-

277 out vertical diffusion, and when neither convection nor diffusion is active are
 278 $7 \times 10^{-5} \text{ s}^{-1}$, $7 \times 10^{-5} \text{ s}^{-1}$, and $1.3 \times 10^{-6} \text{ s}^{-1}$, respectively. The ice fall
 279 speeds follow Heymsfield and Donner (1990), multiplied by a factor of 1.5.
 280 These changes are regarded as within observational or conceptual uncertain-
 281 ties, given the design of the parameterizations. The changes were chosen to
 282 increase realism of the simulations, particularly with regard to radiation bal-
 283 ance, precipitation, and implied ocean heat transports in AM3 integrations
 284 with prescribed sea surface temperatures (SSTs).

285 *e. Cumulus Convection*

286 Deep cumulus systems consist of deep updraft cells, mesoscale updrafts,
 287 and mesoscale downdrafts (Donner, 1993; Donner et al., 2001; Wilcox and
 288 Donner, 2007). Several modifications have been made in AM3 for com-
 289 putational efficiency or simulation improvement. The plumes in the deep
 290 updraft cells are discretized on the AM3 vertical grid instead of a higher-
 291 resolution cloud grid. With the coarser plume resolution, entrainment coef-
 292 ficients have been increased relative to those in Donner (1993) by a factor
 293 of 1.45. Liquid/frozen-water static energy (conservative without precipita-
 294 tion) is used instead of temperature for plume thermodynamics. Aspects
 295 of the water budget in deep convective systems related to R_m , precipitation
 296 from mesoscale updrafts; E_{me} , condensate transfer from mesoscale updrafts
 297 to large-scale stratiform clouds (cf., Section 3d); C_{mu} , condensation and de-
 298 position in mesoscale updrafts; and C_A , lateral transfer of condensate from

299 deep updraft cells to mesoscale updrafts, have been modified. In particu-
 300 lar, $\frac{R_m}{C_{mu}+C_A}$ and $\frac{E_{me}}{C_{mu}+C_A}$ are 0.55 and 0.05, respectively, compared to 0.50
 301 and 0.10 in Donner (1993). In AM3, 10% of the condensate in the cell up-
 302 drafts at the detrainment level evaporates, while all remaining condensate
 303 that does not fall from the cell updrafts as precipitation is transferred to the
 304 mesoscale updraft. In Donner (1993), 13% of the condensate in the cell up-
 305 drafts that is not removed as precipitation evaporates near the detrainment
 306 level, while 25% evaporates in cell-scale downdrafts and 62% is transferred
 307 to the mesoscale updraft. The Donner (1993) partitionings are based on
 308 observations reported by Leary and Houze (1980). In AM3, the top of the
 309 mesoscale circulation is specified as the level of zero buoyancy (or at a pres-
 310 sure 10 hPa less than the level of zero buoyancy, if the deepest cell top is
 311 above the level of zero buoyancy due to overshooting). The top of mesoscale
 312 circulation is restricted to be no higher than the temperature minimum cor-
 313 responding to the local tropopause. The latter condition was found to be
 314 necessary to prevent excessive water vapor in the stratosphere.

315 The closure for deep cumulus results in heating by cumulus convection
 316 relaxing convective available potential energy (CAPE) toward a threshold
 317 over a relaxation time scale (cf., Eq. (2) in Wilcox and Donner (2007)). The
 318 CAPE threshold is $1,000 \text{ J kg}^{-1}$, and the relaxation time scale is 8 hrs.

319 Shallow cumulus follows Bretherton et al. (2004), modified as in Zhao
 320 et al. (2009), with the empirical non-dimensional parameter controlling the

321 strength of the lateral mixing (c_0 in Eq.(18) in Bretherton et al. (2004)) set
322 to 13.5.

323 Both deep and shallow cumulus diffuse large-scale horizontal momentum
324 in proportion to their mass fluxes, as in GFDL GAMDT (2004). The non-
325 dimensional constant γ in Eq. (1) of GFDL GAMDT (2004), which is a
326 factor with the cumulus mass flux in the term added to the vertical diffusion
327 coefficient, takes the value 0.26 in AM3. The GFDL GAMDT (2004) value
328 is 0.20.

329 Finally, moist adiabatic adjustment (MAA) (Manabe et al., 1965) has
330 been retained, since a saturated atmosphere at grid scale should not be un-
331 stable or moist beyond saturation. The parameterizations for deep and shal-
332 low cumulus do not preclude these conditions, which produce small amounts
333 of precipitation relative to other sources.

334 The changes in the parameter settings for deep and shallow convection
335 are within observational uncertainty and, as with the stratiform parameter
336 settings discussed in Section 3d, resulted in improved realism in key aspects
337 of the atmospheric circulation important for coupled climate modeling, e.g.,
338 implied ocean heat transports.

339 In the AM3 integration described in Section 4a, deep convective cells
340 dominate in the middle and upper troposphere in the tropics, but at pres-
341 sures of 100 to 200 hPa, the mass fluxes in mesoscale updrafts are comparable
342 to those in the cells (Fig. 1). Mesoscale downdrafts have the smallest mass

343 fluxes among the convective components, but can extend to the PBL, where
 344 changes by these downdrafts in thermodynamic and moisture structure can
 345 impact surface fluxes. Shallow cumulus can co-exist with deep convection,
 346 and, though its vertical extent is not imposed, generally is confined below
 347 about 500 hPa. Deep convection can only occur when the level of zero buoy-
 348 ancy is at a pressure less than 500 hPa. Both are called from the same
 349 atmospheric state. In AM3, deep convective precipitation dominates in the
 350 tropics, while stratiform precipitation prevails in the middle latitudes (Fig.
 351 2a). The small values of precipitation associated with MAA indicate that the
 352 other precipitation parameterizations generally preclude the development of
 353 over-saturated, unstable conditions. The mid-latitude maxima in precipita-
 354 tion from the MAA coincide with the edges of the faces of the cubed-sphere
 355 in the dynamical core. Relative to precipitation reported by the Version-2
 356 Global Precipitation Climatology Project (GPCP v.2) (Adler et al., 2003),
 357 AM3 produces 16% excessive precipitation. In CM3, described in Section
 358 4, sea-surface temperatures depart from the observed values specified in the
 359 AM3 integrations when AM3 is coupled to ocean and sea-ice models, with
 360 appreciable effects on precipitation patterns (Fig. 2b). Most notably, a
 361 double inter-tropical convergence zone (ITCZ), not evident in GPCP v.2, is
 362 apparent. This double maxima occurs in all of the parameterized sources
 363 of precipitation, despite wide variations in the ways in which occurrence of
 364 precipitation in these parameterizations is related to large-scale flows. The
 365 departure of CM3 precipitation patterns from AM3 patterns is typical when

366 coupling atmospheric and oceanic GCMs and is evidently a consequence of
367 a chain of interactions between the ocean and atmosphere components (e.g.,
368 Zhang et al., 2007).

369 *f. Aerosols*

370 AM3 calculates the mass distribution and optical properties of aerosols
371 based on their emission, chemical production, transport, and dry and wet
372 removal. The transport processes include advection, convection, and eddy
373 diffusion by turbulence. The chemical production of sulfate includes gas
374 and aqueous-phase oxidation of sulfur dioxide by radicals, ozone, and hy-
375 drogen peroxide, which are calculated explicitly by the chemical mechanism
376 described in Section 3g. Dry deposition includes gravitational settling and
377 impaction at the surface by turbulence. Wet deposition takes into account
378 in- and below-cloud scavenging by large-scale and convective clouds.

379 Anthropogenic and biomass burning emissions of sulfur dioxide, black
380 carbon, and organic carbon are from Lamarque et al. (2010). Dimethyl
381 sulfide (DMS) emission is calculated using an empirical formula as a function
382 of seawater DMS concentration and wind speed at 10 m, as described by Chin
383 et al. (2002).

384 Secondary organic aerosols are produced by terrestrial and oceanic sources.
385 Terrestrial production includes natural and anthropogenic sources. The nat-
386 ural source includes oxidation of terpenes emitted from plants, which yields
387 particulate organics (Dentener et al., 2006). The yield factor varies from

0.11 per molecule at latitudes lower than 20° to 0.55 per molecule at the poles. The anthropogenic source follows Tie et al. (2005), where 10% of the butane oxidized by hydroxyl radicals becomes particulate organics. The oceanic source is O'Dowd et al.'s (2008) organic sea-spray source function. Anthropogenic and natural secondary organic aerosol production is 11.3 and 31.5 Tg yr⁻¹, respectively.

Dust emission follows the parameterization by Ginoux et al. (2001) and is based on the preferential location of sources in topographic depressions. Sea salt particles are emitted from the ocean according to Monahan et al. (1986).

For volcanoes, time-invariant sulfur dioxide emissions are specified to be the total *sulfur* emissions recommended by AeroCom (Dentener et al., 2006) for continuous degassing and (time-averaged) explosive emissions, multiplied by a factor of 0.25. These emissions are injected 500 to 1500 m above volcano tops for explosive emissions and over the upper third of volcanoes for continuously degassing volcanoes and are thus confined to the troposphere. The factor applied is justified by the need to scale the total sulfur emissions to include only sulfur dioxide emissions and to simulate realistic sulfur dioxide and sulfate abundances in otherwise clean regions with volcano sources, noting that considerable uncertainty exists in volcano emissions. Due to the absence of some chemical processes important for the formation of stratospheric volcanic aerosols, e.g., related to carbonyl sulfide, and the absence of direct injection of volcanic aerosols into the stratosphere, a stratospheric

signature for volcanoes is imposed through the specification of a time series of spatial distributions of optical properties, as noted in Section 3a.

Following Cooke et al. (1999), we assume that 80% of black carbon and 50% of organics emitted are hydrophobic, the rest being hydrophilic. Hydrophobic black carbon and organic aerosols undergo aging processes to become hydrophilic with e-folding times of 1.44 and 2.88 days, respectively. Secondary organic aerosols are treated as hydrophilic.

Chemical processes related to aerosol formation are discussed in Section 3g. Aerosols are removed by dry deposition at the surface and by scavenging in stratiform and convective clouds. Dry deposition velocities for aerosols are calculated interactively using a wind-driven resistance method, in which the surface resistance is calculated as an empirical parameter (reflecting surface collection efficiency) divided by the friction velocity (Gallagher et al., 2002).

Cloud scavenging of aerosol species is calculated following Giorgi and Chameides (1985). The fractional removal rate is equal to its in-condensate fraction multiplied by the fractional removal rate of condensate by precipitation. For hydrophilic aerosols, an empirical in-condensate fraction (ranging from 0.07 for dust to 0.3 for sulfate in large-scale clouds, and from 0.12 for dust to 0.4 for sulfate in convective clouds) is prescribed. Below-cloud aerosol washout, for large-scale precipitation only, is parameterized as described by Li et al. (2008).

Interactive simulation of aerosols from emissions in CM3 is a major change in approach from CM2.1 (Delworth et al., 2006), in which aerosol concen-

434 trations were specified. AM3 uses different emissions inventories and optical
 435 properties than AM2. AM3 also includes internal mixing and couples wet
 436 deposition to cloud microphysics. A detailed evaluation of aerosol properties
 437 is beyond the scope of this paper. Here, two fundamental CM3 aerosol prop-
 438 erties, aerosol optical depth (AOD) and co-albedo (ratio of absorption optical
 439 depth to total optical depth), are compared with AERONET observations
 440 to show improved correlation relative to CM2.1. As analyzed in detail by
 441 Ginoux et al. (2006), the CM2.1 aerosol distribution tended to overestimate
 442 AOD in polluted regions, while underestimating biomass-burning AOD by a
 443 factor 2 or more, relative to annual-mean AOD measured by AERONET sun
 444 photometers (Holben et al., 1998) (Figs. 3a and b). Ginoux et al. (2006)
 445 also indicate that sea-salt mass was largely underestimated but compensated
 446 in marine environment by excessive sulfate scattering. The best represented
 447 environment was in dusty regions. Figs. 3c and d show a reduction in these
 448 biases, particularly in biomass burning regions, but also in polluted regions.
 449 Note that the model results are averaged from 1981 to 2000, while most
 450 AERONET sun photometers began to operate in the mid nineties or early
 451 21st century. Since sulfur emission has decreased since the mid-nineties,
 452 simulated AOD values are likely higher than observed. Co-albedo measures
 453 aerosol absorption, and the model absorption has largely decreased from
 454 CM2.1 to CM3, agreeing much better with AERONET to generally within a
 455 factor of two at most stations (Fig. 4). This major change, which is partic-
 456 ularly evident over regions of biomass burning, is due to several factors but

457 primarily a decrease of black-carbon emission. The decrease in black-carbon
 458 emission, from 11 Tg yr⁻¹ in AM2 (Horowitz, 2006) to 8.2 Tg yr⁻¹ in AM3, is
 459 partly compensated by increased absorption due to internal mixing of sulfate
 460 and black carbon. Unlike the direct measurement of AOD by sun photome-
 461 ters, co-albedo is retrieved by an inversion of Almucantar data (Dubovik and
 462 King, 2000), and, to limit error of the retrieved values, only data with AOD
 463 greater than 0.45 are inverted. Thus, AERONET co-albedo is representative
 464 of heavy polluted, but not pristine, environments. Another bias to consider
 465 is that AERONET values are at 440 nm (blue), while the simulated aerosol
 466 properties are only archived at 550 nm (green). The subsequent bias will
 467 depend on the spectral variation of aerosol absorption. In biomass burning,
 468 smoke absorbs more in the green than the blue part of the solar spectrum,
 469 so the model co-albedo at 550 nm should be higher than at 440 nm. In
 470 dusty environments, the opposite should be true. These biases may partially
 471 explain the persisting discrepancies in Figs. 4c and d for CM3.

472 Clear-sky downward shortwave radiation in CM3 is generally larger in
 473 CM3 than CM2.1 and closer to observations from the Baseline Surface Radia-
 474 tion Network (BSRN, <http://gewex-rfa.larc.nasa.gov>) (Fig. 5). The increases
 475 in clear-sky downward shortwave radiation are due to reduced aerosol direct
 476 effects in CM3. Improved agreement of CM3 simulations of downward clear-
 477 sky surface shortwave radiation, optical depths, and co-albedo with BSRN
 478 and AERONET provides strong evidence that the direct effects of aerosols
 479 are more realistically simulated in CM3.

480 Aerosol activation into cloud droplets follows the parameterization de-
 481 tailed in Ming et al. (2006). Sulfate and sea salt aerosols are treated as pure
 482 ammonium sulfate and sodium chloride, respectively, in terms of cloud con-
 483 densation nuclei efficiency, while organic aerosol is assumed to be partially
 484 soluble (Ming and Russell, 2004). Black carbon is assumed to be insoluble
 485 and externally mixed with soluble species. However, sulfate and black car-
 486 bon are treated as an internal mixture for radiation calculations. The size
 487 distributions of organic and sea salt aerosols remain unchanged regardless of
 488 ambient conditions. Sulfate is assumed to be entirely in the accumulation
 489 mode if its concentration is above $0.3 \mu\text{g m}^{-3}$. Otherwise, it is partitioned be-
 490 tween the nucleation and accumulation modes depending on the abundance
 491 of primary aerosols (i.e., organics, sea salt, black carbon, and dust). The
 492 fraction of sulfate mass in the nucleation mode is 1 when the concentration
 493 of primary aerosols is less than $0.5 \mu\text{g m}^{-3}$, and decreases linearly to 0 when
 494 it exceeds $1.0 \mu\text{g m}^{-3}$. This choice is based upon the consideration that
 495 that gas-to-particle conversion in polluted conditions occurs mainly through
 496 condensation onto pre-existing particles, as opposed to nucleation.

497 Updraft velocities at cloud base and at the time of cloud formation are
 498 used to drive aerosol activation within shallow cumulus and stratiform clouds,
 499 respectively. Vertical velocities for shallow cumulus are provided directly
 500 by the Bretherton et al. (2004) shallow cumulus parameterization. The
 501 procedure for generating the probability distribution functions for updraft
 502 velocities in stratiform clouds is described in Section 3d. Due to the absence

503 of ice nucleation and limited treatment of microphysics generally in deep
504 convection (in which substantial vertical accelerations can occur well above
505 cloud base, leading to activation above cloud base), aerosol activation is not
506 treated in deep convection. The consequences of this omission are not clear,
507 and the matter is a high priority for future research.

508 A major motivation for including aerosol activation in AM3 is to enable
509 simulation of cloud droplet sizes, which in turn partially determine the ra-
510 diative and macrophysical properties of clouds, i.e., aerosol indirect effects.
511 Droplet sizes have been evaluated using a simple simulator for the Moderate
512 Resolution Imaging Spectroradiometer (MODIS) (King et al., 2003) satellite.
513 For every sub-grid column generated with the stochastic cloud scheme of Pin-
514 cus et al. (2005) and Pincus et al. (2006), cf. Section 3a, the radii for these
515 liquid cloud layers in the top two units of cloud optical depth are averaged
516 to produce a MODIS-like cloud-top radius. All cloudy sub-grid columns are
517 given equal weight in calculating the grid-mean radius.

518 Many general patterns from MODIS (Collection 5) are captured in AM3,
519 including increases in droplet sizes in the oceans off the east coasts of most
520 continents and the January-to-July decrease in droplet sizes over sub-tropical
521 South America and Africa (Fig. 6). The amplitudes of the changes are
522 generally smaller in AM3 than in MODIS, though.

523 *g. Tropospheric and Stratospheric Chemistry*

524 In AM3, the chemistry models of Horowitz et al. (2003) for the tro-

525 posphere and Austin and Wilson (2006) for the stratosphere are merged.
526 The chemical system is solved using a fully implicit Euler backward method
527 with Newton-Raphson iteration, as in Horowitz et al. (2003). Merging the
528 two models consisted mainly of augmenting the tropospheric model with
529 species (including halogens and atomic hydrogen) and reactions, primarily
530 gas-phase halogen reactions, stratospheric and mesospheric photolysis reac-
531 tions, and heterogeneous reactions on stratospheric aerosols. Heterogeneous
532 reactions are also included on polar stratospheric clouds (PSCs), described
533 in the next paragraph. Reaction rates follow recommendations from Sander
534 et al. (2006). The oxidation of sulfur dioxide and dimethyl sulfide to form
535 sulfate aerosol is fully coupled with the gas-phase chemistry. Clear-sky pho-
536 tolysis frequencies are calculated using a multivariate interpolation table de-
537 rived from the Tropospheric Ultraviolet-Visible radiation model (Madronich
538 and Flocke, 1998), with an adjustment applied for the effects of large-scale
539 clouds, as described by Brasseur et al. (1998).

540 Monthly mean dry-deposition velocities for gas-phase species (except for
541 ozone and peroxyacetyl nitrate, PAN) are from Horowitz et al. (2003) and
542 were calculated off-line using resistance in series (Wesely, 1989; Hess et al.,
543 2000). Deposition velocities for ozone were taken from Bey et al. (2001)
544 and those for PAN from a MOZART-4 simulation in which it was calculated
545 interactively to reflect the updates described by Emmons et al. (2010).

546 Cloud scavenging of gas-phase species is treated as for aerosols (Section
547 3f), except the in-condensate fraction is determined by Henry’s law equilib-

rium. Below-cloud washout is calculated only for large-scale precipitation
and is based on Henry’s law, as in Brasseur et al. (1998).

Halogens are treated in a similar manner to Austin and Wilson (2006),
described further in Austin and Wilson (2010). Specifically, the rates of
change of inorganic chlorine and inorganic bromine are parameterized to
minimize the need to transport additional tracers in the model. Also as
described in Austin and Wilson (2010), heterogeneous reactions are included
on ice and nitric acid trihydrate PSCs and in liquid ternary solution (LTS)
aerosols. The PSCs are taken to be in thermodynamic equilibrium with
the local conditions and calculated as in Hanson and Mauersberger (1988).
The reaction rates in LTS are treated as in Carslaw et al. (1995). Mass
accommodation coefficients and reaction probabilities are taken from Sander
et al. (2006).

Compared to the Randel and Wu (2007) climatology, general features of
the annual-mean, zonally averaged ozone for the period 1980-1999 are well
produced with a tropical peak near 10 hPa but with much lower ozone in the
middle and high latitudes (Fig. 7). The tropical concentration peak is slightly
larger than observed, at just over 11 ppmv, compared with the observed 10.5
ppmv, but there is insufficient ozone in the high latitudes, which is likely
related to model transport. The seasonal variation of total column ozone
(Fig. 8) is very similar to Total Ozone Mapping Spectrometer (TOMS)
(Stolarski and Frith, 2006) for the decades of the 1980s and 1990s. In the
1980s, before significant ozone destruction, the model shows low tropical

571 ozone, consistent with observations throughout the year. In middle and high
 572 latitudes, the annual variation is well reproduced, but the column ozone
 573 amounts are biased low in high northern latitudes, reflecting the bias shown
 574 in Fig. 7. In the Southern Hemisphere, the peak column amounts in spring
 575 near 60°S are simulated to be larger than observed. Similar features are
 576 also present in the 1990s. The simulated ozone hole is deeper than observed
 577 and lasts longer into summer, although it is smaller in physical area. In
 578 the annual mean, the biases are generally small (Fig. 8e), under 5%, but
 579 are larger in the Southern Hemisphere and dominated by the spring period
 580 indicated above.

581 **4. Basic Simulation Characteristics**

582 *a. Boundary conditions and integrations*

583 AM3 and the land model were integrated with prescribed sea-surface tem-
 584 peratures, sea-ice coverage, and sea-ice albedo to demonstrate their behavior
 585 with realistic boundary conditions. These integrations will be contrasted in
 586 this section with observations and with simulations in which AM3 served as
 587 the atmospheric component of CM3.

588 Observed sea-surface temperatures and sea ice for the uncoupled integra-
 589 tions are from Rayner et al. (2003). Except as noted below, the period of
 590 integration is 1980 to 2000, with averages taken from 1981 to 2000. Initial
 591 conditions for the atmospheric model are drawn from the AM3 developmental
 592 integrations.

593 For the coupled integrations, CM3 was spun up for several centuries with
 594 1860 trace gas concentrations and emissions, as described in Sections 3a
 595 and 3f. Following the spin-up, time-varying trace gas concentrations and
 596 emissions were imposed over the period 1860-2005. Anthropogenic aerosols
 597 (through both direct and indirect effects) and trace gases force climate be-
 598 tween 1860 and 2000. The CM3 global-mean temperature increased by
 599 0.40°C from the 1881-1920 period to the 1981-2000 period. The correspond-
 600 ing increases in the Climate Research Unit (CRU) observations (Brohan et
 601 al., 2006) and a five-member CM2.1 ensemble (Knutson et al., 2006) were
 602 0.56°C and 0.66°C , respectively. Observed warming is intermediate between
 603 the CM2.1 and CM3 warming. Only a single ensemble member of the cou-
 604 pled integration is considered in this paper. Consequently, CM3 analyses are
 605 restricted to 1981-2000 averages. Considerable inter-ensemble variability is
 606 likely at higher time resolution.

607 *b. Radiation and Surface Fluxes*

608 Annual-mean short-wave absorption by the earth-atmosphere system in
 609 AM3 and the Earth Radiation Budget Experiment (ERBE) (Harrison et al.,
 610 1990) (Fig. 9) agree within 5 W m^{-2} over most of North America, the cen-
 611 tral Pacific Ocean, and southern Europe. AM3 exhibits negative biases in
 612 the tropical Indian and western Pacific Oceans, where excessive cloudiness
 613 and precipitation occur. Positive biases characterize the oceans off the sub-
 614 tropical west coasts of Africa, South America, and North America, where

615 marine stratus is inadequate. Problematic marine stratus persists from AM2
 616 (GFDL GAMDT, 2004), perhaps not surprisingly, given that the parameter-
 617 izations for boundary layers and cloud macrophysics have not been changed
 618 in ways expected to remedy this deficiency. The marine stratocumulus bi-
 619 ases are slightly smaller in the CM3 integrations than the AM3 integrations,
 620 suggesting a response to a small change in SSTs. Simultaneously, negative
 621 biases in the tropical oceans, consistent with a double ITCZ, emerge in the
 622 CM3 integration. A positive bias over the Amazon, consistent with insuffi-
 623 cient convection, is considerably more apparent in the CM3 integration than
 624 in the AM3 integration. The behavior of the corresponding fields for out-
 625 going longwave radiation (OLR) is consistent with the short-wave changes
 626 (Fig. 10). The corresponding fields for outgoing longwave radiation (OLR)
 627 are consistent with the short-wave changes in regions of deep convection.
 628 (Fig. 10). In particular, the AM3 OLR exhibits negative biases in the trop-
 629 ical Indian Ocean and west Pacific, where excessive high cloudiness occurs
 630 in association with deep convection (Fig. 10c). The double ITCZ in CM3
 631 is evident in the splitting of the negative tropical OLR bias in the Pacific
 632 Ocean, separated by a zone of positive bias (Fig. 10d). The positive OLR
 633 bias over the Amazon in CM3 results from insufficient high cloudiness and
 634 convection (Fig. 10d).

635 To present a statistical summary of the radiation balances in AM3 and
 636 CM3, Taylor diagrams (Gates et al., 1999; Taylor, 2001) (Fig. 11) are con-
 637 structed using ERBE observations from 1985-1989 (Harrison et al., 1990)

638 and observations from the Clouds and the Earth's Radiant Energy System
 639 (CERES) satellites from 2000-2005. The CERES observations are analyzed
 640 in several ways: CERES-ES4-ERBE-like, CERES-SRB-GEO, CERES-SRB-
 641 nonGEO (Wielicki et al., 1996), and CERES-Energy Balanced and Filled
 642 (EBAF) (Loeb et al., 2009). (Observations available at [http://eosweb.larc.nasa.gov/](http://eosweb.larc.nasa.gov/PRODOCS/ceres)
 643 PRODOCS/ceres). Shortwave and net radiation have similar root-mean-
 644 square (RMS) errors and correlation relative to observations for both AM3
 645 and CM3. ERBE and CERES observations differ by about as much as the
 646 modeled results do from the CERES results, and the various CERES anal-
 647 yses differ little among themselves. AM3 and CM3 OLR RMS differences
 648 from ERBE are two to three times larger than those of shortwave and net
 649 radiation. Note that the RMS differences in Fig. 11 are normalized by the
 650 standard deviation of the ERBE observations and that the ERBE shortwave
 651 standard deviation is also two to three times larger than that of the ERBE
 652 OLR. The spread among the CERES observations themselves is somewhat
 653 greater for shortwave and longwave cloud forcing (Figs. 11d and e) than
 654 for shortwave radiation and OLR, as are the differences between ERBE and
 655 CERES observations. AM3 and CM3 differ more between themselves than
 656 they did for OLR and shortwave radiation, consistent with the cloud dif-
 657 ferences between AM3 and CM3 evident in Figs. 9c, 9d, 10c, and 10d, for
 658 example, in the ITCZ and regions of marine stratus. Pincus et al. (2008)
 659 note that cloud forcing is a more difficult field for models to simulate than
 660 total fluxes, which are to an appreciable extent controlled by the geometry of

661 solar insolation. In that light, it is noteworthy that shortwave cloud forcing
 662 in AM3 compares more favorably with ERBE and CERES than AM2 (Fig.
 663 11d). Correlations and root mean square differences between both atmo-
 664 spheric models and observations are comparable for longwave cloud forcing,
 665 but AM3 has more spatial variability than observed, while AM2 has less.

666 AM3 and CM3 include the Cloud Feedback Model Intercomparison Project's
 667 Observation Simulator Package (COSP, <http://cfmip.metoffice.com/>). Among
 668 its components, the package includes simulators for the CALIPSO satellite
 669 lidar (Chepfer et al., 2008) and CloudSat radar (Bodas-Salcedo et al., 2008)
 670 which permit comparison of model cloud fields to the vertical structure of
 671 clouds provided by these new instruments. As an example, CALIPSO ob-
 672 servations of cloud fraction for January 2007 (Chepfer et al., 2010) and the
 673 simulated cloud fractions from AM3 show broad, qualitative agreement, while
 674 showing biases consistent with other fields sensitive to cloudiness (Fig. 12).
 675 For example, AM3 simulates smaller cloud fractions than CALIPSO observes
 676 off the west sub-tropical coasts of North America, South America, and Africa,
 677 consistent with positive ERBE shortwave biases in these regions (Figs. 9c
 678 and d).

679 For coupling AM3 with ocean models, the surface energy balance (includ-
 680 ing latent and sensible heat fluxes, in addition to radiative fluxes) is crucial
 681 and not related trivially to the top-of-atmosphere radiation balance. The
 682 implied ocean heat transport (OHT) is the heat transport implied in the
 683 ocean to balance surface fluxes. Although considerable uncertainty exists in

684 diagnosing implied ocean heat transports from observations (e.g., Large and
685 Yeager, 2009; Griffies et al., 2009), agreement between these transports in
686 uncoupled atmospheric models and observational estimates has been found
687 to favor successful coupling with ocean models. The AM3 implied OHT
688 generally fall within or close to observational estimates of Ganachaud and
689 Wunsch (2003) and Trenberth and Caron (2001), except for the Indo-Pacific
690 Ocean south of 30°S (Fig. 13).

691 *c. Dynamics*

692 AM3’s mid-latitude westerly jets in the troposphere are about 10% stronger
693 than in the ERA-40 re-analysis (Uppala et al., 2005) (Fig. 14). A small area
694 of weak, spurious westerlies appears in the equatorial stratosphere around 10
695 hPa, and stratospheric westerlies at polar latitudes can be over 50% stronger
696 than in ERA-40. In the troposphere, westerly biases are smaller in CM3 than
697 AM3 in the Southern Hemisphere but larger in the Northern Hemisphere.

698 Wind stresses in uncoupled models, along with implied OHT, are im-
699 portant to successful coupling. Wind stresses over the Atlantic and Pacific
700 Oceans for AM3 and CM3 are generally within or close to the observational
701 estimates from the Comprehensive Ocean-Atmosphere Data Sets (COADS)
702 (da Silva et al., 1994; Woodruff et al., 1987), ECMWF re-analysis (Gibson et
703 al., 1997), and the ERS satellite scatterometer (CERSAT-IFREMER, 2002)
704 (Fig. 15). The largest AM3 Pacific departures from observations are in the
705 Southern Hemisphere, where CM3 stresses agree better with observations.

706 The largest Atlantic departures for CM3 are in the Northern Hemisphere,
707 where AM3 agrees better with observations.

708 In AM3, Northern Hemisphere December-January-February (DJF) sea-
709 level pressures (SLP) are biased high over most of the middle latitudes with
710 a mixed difference pattern in the Arctic, compared to the NCEP-NCAR re-
711 analysis (Kalnay et al., 1996) (Fig. 16). CM3 differences over the Atlantic
712 are similar in pattern to AM3 but larger in magnitude, but a negative bias
713 characterizes the Pacific. The maximum positive bias in the Arctic is less
714 than half as large as in AM2 (cf., Fig. 6 in GFDL GAMDT (2004)).

715 The magnitudes of the errors in the DJF stationary waves (time-mean
716 departures of the 500 hPa geopotential height from its zonal mean) are no-
717 ticeably larger in CM3 than AM3 (Fig. 17). The amplitudes of the waves are
718 larger over Europe, east Asia, and northeast North America in CM3, and the
719 waves are shifted slightly eastward over North America in CM3, relative to
720 AM3. In the Southern Hemisphere, the magnitudes of the departures from
721 the zonal mean are generally larger in AM3.

722 A measure of the AM3's skill in simulating a key aspect of the El Niño-
723 Southern Oscillation is its modeled relationship between tropical SST and
724 the global precipitation pattern. This pattern can be depicted as the prod-
725 uct of the standard deviation of the Niño-3 index and regression coefficients
726 between the Niño-3 index and precipitation. This pattern corresponds to
727 AM3's precipitation response to a temperature anomaly of one standard de-
728 viation in the Niño-3 region. (The Niño-3 index is the average SST anomaly

729 over the region 5°S-5°N, 150°-90°W.) Although the patterns in both AM3
730 and CM3 appear to be more zonal than those based on the GPCP analysis
731 (Huffman et al., 1997), broad features of the observed pattern are simulated
732 (Fig. 18).

733 AM3's skill in simulating temperature and pressure patterns associated
734 with the Northern Annular Mode (NAM), also referred to as the Arctic Os-
735 cillation, can be similarly assessed. These patterns can be depicted as the
736 product of the standard deviation of the NAM index and the regression co-
737 efficients between the NAM index and the field of interest. (The NAM index
738 is the first principal component of April-November monthly SLP north of
739 20°N.) The basic structures of temperature and pressure anomalies are sim-
740 ilar in AM3 and observations, with magnitudes of AM3 pressure anomalies
741 somewhat smaller (larger) than observed over Greenland and Asia (North
742 Pacific) (Fig. 19). The magnitudes of temperature anomalies in AM3 are
743 larger than observed at high latitudes and over the Pacific.

744 The frequency of tropical cyclones, diagnosed using the method of Vitart
745 et al. (1997), with observations from the U.S. National Hurricane Center
746 (<http://www.nhc.noaa.gov/pastall.shtml#hurdat>) for the Atlantic and east-
747 ern north Pacific and from the U.S. Navy ([http://www.usno.navy.mil/NOOC/nmfc-](http://www.usno.navy.mil/NOOC/nmfc-ph/RSS/jtwc/best_tracks)
748 [ph/RSS/jtwc/best_tracks](http://www.usno.navy.mil/NOOC/nmfc-ph/RSS/jtwc/best_tracks)) for other basins, is greater than simulated in AM3
749 and CM3 (Fig. 20), although many features of their distribution are cap-
750 tured. Total tropical cyclone frequencies are 28.2, 37.7, and 87.7 storms per
751 year for AM3, CM3, and observations, respectively. The frequency of storms

752 in CM3 is 1.34 times that of AM3, consistent with the sensitive dependence
 753 of the behavior of tropical cyclones on the details of SST in models with
 754 much higher resolution and greater capabilities for cyclone simulation (Zhao
 755 et al., 2009; Bender et al., 2010).

756 The AM3 tropical (15°S to 15°N) wave spectrum has been evaluated
 757 in the format of Wheeler and Kiladis (1999). AM3 is essentially without
 758 Kelvin waves or a Madden-Julian Oscillation (MJO) in contrast to the anal-
 759 ysis based on OLR observations (Liebmann and Smith, 1996) (Fig. 21a,c).
 760 The simulated tropical wave spectrum is very sensitive to the closure and
 761 trigger used for the deep-cumulus parameterization (Lin et al., 2006). In
 762 experimental integrations with AM3, the CAPE relaxation closure described
 763 in Section 3e was replaced by Zhang’s (2002) closure and a trigger requiring
 764 time-integrated low-level lifting sufficient to move a parcel from the bound-
 765 ary layer to the level of free convection (cf., Eqs. (6) and (7) in Donner et
 766 al. (2001)). Zhang’s (2002) closure balances changes in CAPE by convec-
 767 tion with changes in CAPE by non-convective processes above the PBL, i.e.,
 768 CAPE changes arising only from changes in the environment of a cumulus
 769 parcel. Effectively, Zhang’s (2002) closure imposes a balance between the
 770 vertical integrals of large-scale advection of dry static energy and convective
 771 heating (Zhang, 2009). Use of the Zhang (2002) closure with a lifting trigger
 772 produces a stronger Kelvin wave and MJO, though both remain weaker than
 773 observed (Fig. 21b). The closure and trigger for the cumulus parameteriza-
 774 tion impact many aspects of the simulated general circulation. For example,

775 unlike the tropical-wave spectrum, the annual-mean precipitation is more re-
 776 alistic in AM3 with the CAPE relaxation closure. The promising simulation
 777 of the tropical wave spectrum (and evidence in its favor from field programs,
 778 e.g., Zhang (2002) and Donner and Philips (2003)), suggest further research
 779 as to its impact on other aspects of ocean-atmosphere coupled simulations
 780 as a high priority. (These sensitivity experiments are five-year integrations
 781 using climatological 1981-2000 SSTs.)

782 *d. Thermodynamics and Precipitation*

783 Tropospheric temperatures in AM3 and CM3 are generally within 2°C
 784 of ERA-40 re-analysis (Uppala et al., 2005), with CM3 slightly cooler than
 785 AM3 (Fig. 22). Except in polar regions at pressures greater than 5 to 10
 786 hPa, AM3 and CM3 stratospheric temperatures are generally higher than
 787 those of ERA-40.

788 Compared to observed SST ([http://www-pcmdi.llnl.gov/projects/amip/](http://www-pcmdi.llnl.gov/projects/amip/AMIP2EXPDSN/BCS_OBS/amip2.bcs.htm)
 789 [AMIP2EXPDSN/BCS_OBS/amip2.bcs.htm](http://www-pcmdi.llnl.gov/projects/amip/AMIP2EXPDSN/BCS_OBS/amip2.bcs.htm)), warm biases in CM3 are evi-
 790 dent off the sub-tropical west coasts of North and South America and Africa
 791 (Fig. 23), consistent with low-cloud errors also apparent in absorbed short-
 792 wave radiation (Fig. 9c and d). Warm biases north of Antarctica are con-
 793 sistent with shortwave errors in CM3, which develop as a result of ocean-
 794 atmosphere coupling (Fig. 9c and d). A broad cold bias of 2 to 3 °C prevails
 795 over the middle latitudes of the west and central Pacific, and a complex
 796 error pattern of varying signs, associated with details of the Gulf Stream

797 simulation, characterizes the North Atlantic.

798 Both AM3 and CM3 capture general features of CRU temperature obser-
799 vations (Brohan et al., 2006) at 2m over land areas (Fig. 24). Eurasia, North
800 America, and Africa are slightly cooler in CM3 than in AM3. Excessive vari-
801 ability of these temperatures compared to CRU observations is reduced in
802 CM3, relative to CM2 (Table 2).

803 AM3 precipitation in tropical oceans is excessive compared with GPCP
804 v. 2 observations (Adler et al., 2003), by as much as 3 to 5 mm d⁻¹. (Fig.
805 25). Relative to AM2.1, the AM3 Amazon simulation has improved markedly
806 (cf., Fig. 17, Delworth et al., 2006), and reduced the summer dry bias in the
807 southern Great Plains of North America. CM3 develops a double ITCZ,
808 which is considerably less evident in AM3. A moist bias over the western
809 United States and a dry bias over northern South America develop in CM3
810 but are not evident in AM3. A moist bias over southern Africa is stronger in
811 CM3 than AM3. As for the tropical-wave spectrum (Fig. 21), the distribu-
812 tion of precipitation intensity depends strongly on the closure and triggers for
813 deep convection. As an example, the CAPE-relaxation closure used in AM3
814 fails to capture observed high-intensity precipitation events over tropical land
815 areas (Fig 26). The closure balancing convective changes in CAPE against
816 changes in CAPE due to changes in the environment of cumulus parcels,
817 in conjunction with a low-level lift trigger, does so. (The observed distri-
818 bution of precipitation intensities is based on the Special Sensor Microwave
819 Imager (SSM/I) aboard the Defense Meteorological Satellite Program F13

820 and F14 satellites and the Tropical Rainfall Measuring Mission Microwave
821 Imager (TMI) (Wilcox and Donner, 2007).) As noted in Section 4c, future
822 research on alternatives to the CAPE-relaxation closure is planned.

823 5. Conclusion

824 AM3 and CM3 have been formulated to enable study of several issues in
825 climate and climate change which could be addressed in only limited ways
826 with earlier GFDL coupled GCMs. These issues include cloud-aerosol inter-
827 actions in the climate system, tropospheric and stratospheric chemistry, and
828 interactions between the troposphere and stratosphere which have been iden-
829 tified as important in decadal variability (e.g., Southern Hemisphere Annular
830 Mode). AM3 has increased vertical resolution and extent in its stratosphere,
831 relative to AM2.

832 Despite major changes in the dynamical core and parameterizations for
833 cloud microphysics (physically based aerosol activation), cloud macrophysics
834 (sub-grid vertical velocities, used for aerosol activation), and deep and shal-
835 low cumulus convection, overall statistics characterizing key climate fields
836 change only slightly relative to AM2 and CM2.1 (Fig. 27). AM3 compares
837 favorably to models in the Atmospheric Model Intercomparison Program
838 (AMIP) at the Project for Climate Model Diagnosis and Intercomparison
839 (PCMDI) for phase 3 of the Climate Model Intercomparison Project (CMIP3)
840 (Meehl et al., 2007), whose coupled simulations have performed well (Reichler
841 and Kim, 2008). Relative to AM2 and CM2.1, several notable improvements

842 in AM3 and CM3 are not evident in Fig. 27, as discussed elsewhere: (1) AM3
843 has a smaller Amazon precipitation bias (important for future coupling with
844 a carbon-cycle model) and summer dry bias in the North American southern
845 Great Plains. (2) AM3’s simulation of shortwave cloud forcing agrees bet-
846 ter with ERBE and CERES observations than AM2’s. (3) The simulation of
847 Arctic SLP and sea ice in CM3 have improved relative to CM2.1. (4) Aerosol
848 direct effects are more realistic in AM2, as evidenced by better agreement of
849 clear-sky downward shortwave radiation with BSRN and optical depths and
850 co-albedos with AERONET.

851 The evolution of CM3 with aerosol-cloud interactions from pre-industrial
852 to present-day conditions produces global and regional temperature patterns
853 that are realistic during the late 20th century (Figs. 22, 23, 24, and 27).
854 CM3 treats both direct and indirect aerosol effects (aerosol-cloud interac-
855 tions). CM2.1, which treated only direct aerosol effects, also simulated the
856 climate of the late 20th century realistically (Knutson et al., 2006) but did
857 so without including aerosol-cloud interactions, which produce cooling. Both
858 CM2.1 and CM3 achieve realistic late-20th century global temperatures by
859 offsetting anthropogenic warming by greenhouse gases with aerosol effects. In
860 CM3, the aerosols act both directly and through cloud-aerosol interactions,
861 while in CM2.1 aerosols acted only through direct effects. Together, the
862 increased realism of CM3’s direct aerosol effect relative to CM2.1 and the
863 general agreement of CM3’s late-20th century warming with observations
864 suggest that CM3’s treatment of aerosol indirect effects is more plausible

865 than the absence of aerosol indirect effects in CM2.1.

866 AM3 simulates key observed features of the stratospheric ozone distribu-
867 tion and the evolution of the stratospheric ozone hole.

868 High-priority future development should address ongoing biases in sub-
869 tropical marine stratus in both AM3 and CM3. The emergence of a double
870 ITCZ and dry bias in the Amazon when AM3 is coupled to an ocean model
871 is also an important deficiency. Improved simulation of the intensity of the
872 precipitation distribution and tropical waves, especially the MJO, also de-
873 serves attention. Addressing biases in marine stratus will require changing
874 the behavior of stratiform macrophysics, most likely by a combination of
875 changes in vertical resolution and formulation (Guo et al., 2010). The clo-
876 sure for the cumulus parameterization appears to be a promising target for
877 increased realism of higher-frequency variability and precipitation intensity.
878 The implementation of aerosol-cloud interactions in AM3 does not include
879 deep convective clouds or ice clouds. Emphasis should be placed on improv-
880 ing the physical realism of convective microphysics and ice microphysics, with
881 double-moment microphysics offering advantages of consistent treatment of
882 ice and liquid particles. With respect to the stratosphere, improvements in
883 the parameterization of gravity waves are required, and the absence of a
884 quasi-biennial oscillation is a serious deficiency requiring attention.

885 *Acknowledgments.* We thank Jeff Varanyak for assisting with figure prepa-
886 ration. Reviews of an early draft by Tom Delworth and Gabriel Lau are

887 appreciated.

888 We acknowledge the modeling groups, PCMDI, and the World Climate
889 Research Program's (WCRP's) Working Group on Coupled Modelling for
890 their roles in making available the WCRP CMIP3 multi-model dataset. Sup-
891 port of this dataset is provided by the Office of Science, U.S. Department of
892 Energy.

893 The contribution of Stephen A. Klein to this work was funded through
894 the Regional and Global Climate Modeling and Atmospheric System Re-
895 search Programs of the Office of Science in the U. S. Department of En-
896 ergy and was performed under the auspices of the U. S. Department of
897 Energy by Lawrence Livermore National Laboratory under Contract DE-
898 AC52-07NA27344. Robert Pincus was supported by the Office of Science,
899 U.S. Department of Energy, under contract DE FG02-03ER63561. Yanluan
900 Lin was supported by the Office of Biological and Environmental Research,
901 U.S. Department of Energy, under Project Project 0013852.

902 We thank the AERONET principal investigators and their staffs for es-
903 tablishing and maintaining the AERONET sunphotometer sites used in this
904 investigation.

APPENDIX 1

CM3 Land, Ocean, and Sea-Ice Models

905 *a. Land Model*

906 LM3, the land model coupled to AM3, is a new model for land water,
907 energy, and carbon balance. In comparison to its predecessor (the Land
908 Dynamics, or LaD, model (Milly and Shmakin, 2002)), LM3 includes a
909 multi-layer model of snow pack above the soil; a continuous vertical rep-
910 resentation of soil water that spans both the unsaturated and saturated
911 zones; a frozen soil-water phase; a parameterization of water-table height,
912 saturated-area fraction, and groundwater discharge to streams derived from
913 standard groundwater-hydraulic assumptions and surface topographic infor-
914 mation; finite-velocity horizontal transport of runoff via rivers to the ocean;
915 lakes, lake ice, and lake-ice snow packs that exchange mass and energy with
916 both the atmosphere and the rivers; and consistent, energy-conserving ac-
917 counting of sensible heat content of water in all its phases. Carbon balance
918 and the determination of vegetation structure, phenology, and function are
919 accomplished as in the model LM3V (Shevliakova et al., 2009).

920 In stand-alone numerical experiments with observation-based atmospheric
921 forcing, and in experiments coupled to AM2 and AM3, LM3 preserves the
922 generally realistic water-balance partitioning of the LaD model; ameliorates
923 some of the deficiencies of the LaD model previously identified; and provides
924 qualitatively realistic estimates of physical variables that are not tracked by

925 the LaD model.

926 *b. Ocean Model*

927 The ocean model component of CM3 uses the MOM4p1 code (Griffies,
928 2009), whereas the ocean component of CM2.1 used the MOM4.0 code (Griffies
929 et al., 2005). The physical parameterizations and grid resolution for the
930 CM3 ocean are the same as that used in CM2.1, as detailed in Griffies et
931 al. (2005) and Gnanadesikan et al. (2006). The single change made for
932 CM3 concerns the numerical formulation of the vertical coordinate (Griffies
933 et al., 2010). Tests with the new vertical coordinate in CM2.1 showed triv-
934 ial climate changes to the simulation as described, for example, in Delworth
935 et al. (2006) and Gnanadesikan et al. (2006). Hence, for purposes of the
936 present paper, the ocean component can be considered the same as that used
937 in CM2.1.

938 *c. Sea-Ice Model*

939 The CM3 sea-ice is identical to that in CM2.1 (Delworth et al., 2006;
940 Winton, 2000), except for some parameter resetting made possible by im-
941 proved realism in CM3’s climate in regions of sea ice. The dry snow and
942 ice albedos in CM3 are 0.85 and 0.68, respectively. These albedos are more
943 realistic (Perovich et al., 2002) than the corresponding values of 0.80 and
944 0.58 in CM2.1. The decrements to these values for melting are ramped lin-
945 early between a threshold skin temperature of 1° C below freezing in CM3
946 (compared to 10° C below freezing in CM2.1), and the freezing point.

947 Compared to observations (Hurrell et al., 2008) CM3 sea ice extent is
948 too far south in areas of the North Atlantic east of Greenland (Fig. A1).
949 In general, the simulation of Northern Hemisphere sea ice has improved in
950 CM3 relative to CM2.1, but Southern Hemisphere ice concentrations remain
951 smaller than observed (cf., Fig. 9, Griffies et al., 2010).

APPENDIX 2

Symbols and Units

<i>Symbol</i>	<i>Description</i>	<i>Units</i>
a_k	constant used to calculate pressure at interface k	Pa
b_k	constant used to calculate pressure at interface k	dimensionless
c_0	lateral mixing constant for shallow cumulus	dimensionless
C_A	vertically integrated lateral transfer of condensate from updraft cells to mesoscale updrafts	$\text{kg m}^{-2} \text{s}^{-1}$
C_{mu}	vertically integrated condensation and deposition in mesoscale updrafts	$\text{kg m}^{-2} \text{s}^{-1}$
D	rate of change of saturated cloud mass flux with pressure in detraining layers	s m^{-1}
E_{me}	vertically integrated condensate transfer from mesoscale updrafts to large-scale stratiform clouds	$\text{kg m}^{-2} \text{s}^{-1}$
g	gravity constant	m s^{-2}
M	mass flux	$\text{kg m}^{-2} \text{s}^{-1}$
p	pressure	Pa
R_m	precipitation rate from mesoscale updrafts	$\text{kg m}^{-2} \text{s}^{-1}$
X	mixing ratio for cloud liquid or ice; cloud fraction	$\text{kg}(\text{water}) \text{kg}^{-1}$; dimensionless
z	height	km
γ	factor relating cumulus mass flux to vertical diffusion coefficient for momentum	dimensionless

952 The following apply generally:

953 $()_{deep}$ refers to deep convective systems, comprised of cells and mesoscale
954 circulations.

955 $()_{meso}$ refers to mesoscale updrafts.

956 $()_{shal}$ refers to shallow cumulus.

957 $()_s$ refers to lower boundary of atmospheric model.

958 $()^*$ refers to a property or process within a convective system.

959 $\overline{()}$ refers to a large-scale average.

REFERENCES

- 960 Adler, R.F., G.J. Huffman, A. Chang, R. Ferraro, P.-P. Xie, J. Janowiak, B.
 961 Rudolf, U. Schneider, S. Curtis, D. Bolvin, A. Gruber, J. Susskind, P.
 962 Arkin, and E. Nelkin, 2003: The version-2 global precipitation climatol-
 963 ogy project (GPCP) monthly precipitation analysis (1979-present). *J.*
 964 *Hydrometeorology*, **4**, 1147-1167.
- 965 Alexander, M.J., and T.J. Dunkerton, 1999: A spectral parameterization of
 966 mean-flow forcing due to breaking gravity waves. *J. Atmos. Sci.*, **56**,
 967 4167-4182.
- 968 Alexander, M.J., and K.H. Rosenloff, 2003: Gravity-wave forcing in the
 969 stratosphere: Observational constraints from the upper atmosphere re-
 970 search satellite and implications for parameterization in global models,
 971 *J. Geophys. Res.*, **108**, doi:10.1029/2003JD003373.
- 972 Austin, J., and R.J. Wilson, 2006: Ensemble simulations of the decline and
 973 recovery of stratospheric ozone. *J. Geophys. Res.*, **111**, D16314, doi10.1029/2005JD006907.
- 974 —, 2010: Sensitivity of polar ozone to sea surface temperatures and halogen
 975 amounts. *J. Geophys. Res.*, **115**, doi: 10.1029/2009JD013292.
- 976 Balkanski, Y., M. Schulz, T. Claquin, S. and Guibert, 2007: Reevaluation
 977 of mineral aerosol radiative forcings suggests a better agreement with
 978 satellite and AERONET data. *Atmos. Phys. Chem.*, **7**, 81-97.

979 Bender, M.A., T.R. Knutson, R.E. Tuleya, J.J. Sirutis, G.A. Vecchi, S.T.
980 Garner, and I.M. Held, 2010: Modeled impact of anthropogenic warming
981 on the frequency of intense Atlantic hurricanes. *Science*, **327**, 454-454.

982 Bey, I., D. J. Jacob, R. M. Yantosca, J. A. Logan, B. D. Field, A. M. Fiore, Q.
983 Li, H. Y. Liu, L. J. Mickley, and M. G. Schultz, 2001: Global modeling of
984 tropospheric chemistry with assimilated meteorology: Model description
985 and evaluation. *J. Geophys. Res.*, **106**, 23,073-23,095.

986 Bodas-Salcedo, A., M.J. Webb, M.E. Brooks, M.A. Ringer, K.D. Williams,
987 S.F. Milton, D.R. Wilson, 2008: Evaluating cloud systems in the Met
988 Office global forecast model using simulated CloudSat radar reflectivities.
989 *J. Geophys. Res.* **113**, doi:10.1029/2007JD009620.

990 Bower, K.N., T.W. Choulaton, J. Latham, J. Nelson, M.B. Baker, and J.
991 Jensen, 1994: A parameterization of warm clouds for use in atmospheric
992 general circulation models. *J. Atmos. Sci.*, **51**, 2722-2732.

993 Brasseur, G.P., et al., 1998: MOZART, a global chemical transport model for
994 ozone and related chemical tracers: 1. Model description. *J. Geophys.*
995 *Res.*, **103**, 28,265-28,289.

996 Bretherton, C.S., J.R. McCaa, and H. Grenier, 2004: A new parameterization
997 for shallow cumulus convection and its application to marine subtropical
998 cloud-topped boundary layers. Part I: Description and 1D results. *Mon.*

- 999 *Wea. Rev.*, **132**, 864-882.
- 1000 Brohan, P., J.J. Kennedy, I. Harris, S.F.B. Tett and P.D. Jones, 2006: Uncer-
 1001 tainty estimates in regional and global observed temperature changes: a
 1002 new dataset from 1850. *J. Geophys. Res.*, **111**, doi:10.1029/2005JD006548.
- 1003 Carslaw, K.S., B.P. Luo, and Th. Peter, 1995: An analytic expression for the
 1004 composition of aqueous HNO_3 - H_2SO_4 stratospheric aerosols including
 1005 gas phase removal of HNO_3 . *Geophys. Res. Lett.*, **22**, 1877-1880.
- 1006 CERSAT-IFREMER, 2002: ERS-1, ERS-2, and NSCAT. Vol. 1. Mean wind
 1007 fields (MWF product). User manual. C2-MUT-W-05-IF, Brest, France.
 1008 72pp. [Available online at [ftp://ftp.ifremer.fr/ifremer/cersat/documentation/](ftp://ftp.ifremer.fr/ifremer/cersat/documentation/gridded/mwf-ers-vol1.pdf)
 1009 [gridded/mwf-ers-vol1.pdf](ftp://ftp.ifremer.fr/ifremer/cersat/documentation/gridded/mwf-ers-vol1.pdf)]
- 1010 Chepfer, H., S. Bony, D. Winker, M. Chiriaco, J.-L. Dufresne, and G. Séze,
 1011 2008: Use of CALIPSO lidar observations to evaluate cloudiness simu-
 1012 lated by a climate model. *Geophys. Res. Lett.*, **35**, doi:10.1029/2008GL034207.
- 1013 Chepfer, H., S. Bony, D. Winker, G. Cesana, J. L. Dufresne, P. Minnis,
 1014 C. J. Stubenrauch, and S. Zeng, 2010: The GCM-Oriented CALIPSO
 1015 Cloud Product (CALIPSO-GOCCP). *J. Geophys. Res.*, **115**, D00H16,
 1016 doi:10.1029/2009JD012251.
- 1017 Chin, M., P. Ginoux, S. Kinne, O. Torres, B.N. Holben, B.N. Duncan, R.V.
 1018 Martin, J.A. Logan, A. Higurashi, T. and Nakajima, 2002: Tropospheric

1019 aerosol optical thickness from the GOCART model and comparisons with
1020 satellite and Sun photometer measurements. *J. Atmos. Sci.*, **59**, 461-
1021 483.

1022 Cooke, W.F., C. Lioussé, H. Cachier, and J. Feichter, 1999: Construction of
1023 a $1^\circ \times 1^\circ$ fossil fuel emission data set for carbonaceous aerosol and im-
1024 plementation and radiative impact in the ECHAM4 model. *J. Geophys.*
1025 *Res.*, **104**, 137-162.

1026 da Silva, A., A.C. Young, and S. Levitus, 1994: *Algorithms and Procedures.*
1027 *Vol. 1, Atlas of Surface Marine Data 1994*, NOAA Atlas NESDIS 6, 83
1028 pp.

1029 Delworth, T.D., A.J. Broccoli, A. Rosati, R.J. Stouffer, V. Balaji, J.A.
1030 Beesley, W.F. Cooke, K.W. Dixon, J. Dunne, K.A. Dunne, J.W. Du-
1031 rachta, K.L. Findell, P. Ginoux, A. Gnanadesikan, C.T. Gordon, S.M.
1032 Griffies, R. Gudgel, M.J. Harrison, I.M. Held, R.S. Hemler, L.W. Horowitz,
1033 S.A. Klein, T.R. Knutson, P.J. Kushner, A.R. Langenhorst, H.-C. Lee,
1034 S.-J. Lin, J. Lu, S.L. Malyshev, P.C.D. Milly, V. Ramaswamy, J. Rus-
1035 sell, M.D. Schwarzkopf, E. Shevliakova, J.J. Sirutis, M.J. Spelman, W.F.
1036 Stern, M. Winton, A.T. Wittenberg, B. Wyman, F. Zeng, and R. Zhang,
1037 2006: GFDL's CM2 global coupled climate models-Part I: Formulation
1038 and simulation characteristics. *J. Climate*, **19**, 643-674.

1039 Dentener, F., S. Kinne, T. Bond, O. Boucher, J. Cofala, S. Generoso, P.

1040 Ginoux, S. Gong, J. J. Hoelzemann, A. Ito, L. Marelli, J. E. Penner,
1041 J.-P. Putaud, C. Textor, M. Schulz, G. R. van der Werf, and J. Wilson,
1042 2006: Emissions of primary aerosol and precursor gases in the years 2000
1043 and 1750 prescribed data-sets for AeroCom. *Atmos. Chem. Phys.*, **6**,
1044 4321-4344.

1045 Donner, L.J., 1993: A cumulus parameterization including mass fluxes, ver-
1046 tical momentum dynamics, and mesoscale effects. *J. Atmos. Sci.*, **50**,
1047 889-906.

1048 —, C.J. Seman, and R.S. Hemler, 2001: A cumulus parameterization in-
1049 cluding mass fluxes, convective vertical velocities, and mesoscale effects:
1050 Thermodynamic and hydrological aspects in a general circulation model.
1051 *J. Climate*, **14**, 3444-3463.

1052 Donner, L.J., C.J. Seman, B.J. Soden, R.S. Hemler, J.C. Warren, J. Ström,
1053 and K.-N. Liou, 1997: Large-scale ice clouds in the GFDL SKYHI general
1054 circulation model. *J. Geophys. Res.*, **102**, 21,745-21,768.

1055 Donner, L.J., and V.T. Phillips, 2003: Boundary-layer control on convective
1056 available potential energy: Implications for cumulus parameterization.
1057 *J. Geophys. Res.*, **108**, doi:10.1029/2003JD003773.

1058 Dubovik, O. and King, M.D., 2000: A flexible inversion algorithm for re-
1059 trieval of aerosol optical properties from Sun and sky radiance measure-

- 1060 ments. *J. Geophys. Res.*, **105**, doi:10.1029/2000JD900282.
- 1061 Emmons, L.K., et al., 2010: Description and evaluation of the Model for
 1062 Ozone and Related chemical Tracers, version 4 (MOZART-4). *Geosci.*
 1063 *Model Dev.*, **3**, 43-67.
- 1064 Freidenreich, S.M., and V. Ramaswamy, 1999: A new multiple-band solar
 1065 radiative parameterization for general circulation models. *J. Geophys.*
 1066 *Res.*, **104**, 31,389-31,409.
- 1067 Fu, Q., 1996: An accurate parameterization of the the solar radiative prop-
 1068 erties of cirrus clouds for climate models. *J. Climate*, **9**, 2058-2082.
- 1069 —, and K.N. Liou, 1993: Parameterization of the radiative properties of
 1070 cirrus clouds. *J. Atmos. Sci.*, **50**, 2008-2025.
- 1071 Fu, Q., P. Yang, and W.B. Sun, 1998: An accurate parameterization of
 1072 the infrared radiative properties of cirrus clouds for climate models. *J.*
 1073 *Climate*, **11**, 2223-2237.
- 1074 Gallagher, M.W., et al., 2002: Measurements and parameterizations of small
 1075 aerosol deposition velocities to grassland, arable crops, and forest: Influ-
 1076 ence of surface roughness length on deposition. *J. Geophys. Res.*, **107**,
 1077 doi:10.1029/2001JD000817.
- 1078 Ganachaud, A., and C. Wunsch, 2003: Large-scale ocean heat and freshwater

- 1079 transports during the World Ocean Circulation Experiment. *J. Climate*,
1080 **16**, 696-705.
- 1081 Gates, W.L., and Co-Authors, 1999: An overview of the results of the Atmo-
1082 spheric Model Inter-Comparison Project (AMIP I). *Bull. Amer. Meteor.*
1083 *Soc.*, **80**, 29-55.
- 1084 Geophysical Fluid Dynamics Laboratory Global Atmosphere Model Devel-
1085 opment Team, 2004: The new GFDL global atmosphere and land model
1086 AM2-LM2: Evaluation with prescribed SST simulations. *J. Climate*, **17**,
1087 4641-4673.
- 1088 Ghan, S.J., L. R. Leung, R.C. Easter, and H. Abdul-Razzak, 1997: Prediction
1089 of cloud droplet number in a general circulation model. *J. Geophys. Res.*,
1090 **102**, 21,777-21,794.
- 1091 Gibson, J.K., P. Kallberg, S. Uppala, A. Hernandez, A. Nomura, and E.
1092 Serrano, 1997: ERA Description. Vol 1. ECMWF Re-analysis Project
1093 Rep. Series, European Centre for Medium-Range Weather Forecasts,
1094 Reading, United Kingdom, 66 pp.
- 1095 Ginoux, P., M. Chin, I. Tegen, J. M. Prospero, B. Holben, O. Dubovik, and
1096 S. Lin, 2001: Sources and distributions of dust aerosols simulated with
1097 the GOCART model. *J. Geophys. Res.*, **106**, 22055-22074.
- 1098 Ginoux, P., Horowitz, L.W., Ramaswamy, V., Geogdzhayev, I.V., Holben,

1099 B.N., Stenchikov, G. and Tie, X., 2006: Evaluation of aerosol distri-
1100 bution and optical depth in the Geophysical Fluid Dynamics Labora-
1101 tory coupled model CM2.1 for present climate. *J. Geophys. Res.*, **111**,
1102 doi:10.1029/2005JD006707.

1103 Giorgetta, M.A., E. Manzini, R. Roeckner, M. Esch, and L. Bengtsson,
1104 2006: Climatology and forcing of the quasi-biennial oscillation in the
1105 MAECHAM5 model. *J. Climate*, **19**, 3882-3901.

1106 Giorgi, F., and W.L. Chameides, 1985: The rainout parameterization in a
1107 photochemical model. *J. Geophys. Res.*, **90**, 7872-7880.

1108 Gnanadesikan, A., Dixon, K. W., Griffies, S. M., Balaji, V., Beesley, J. A.,
1109 Cooke, W. F., Delworth, T. L., Gerdes, R., Harrison, M. J., Held, I. M.,
1110 Hurlin, W. J., Lee, H.-C., Liang, Z., Nong, G., Pacanowski, R. C., Rosati,
1111 A., Russell, J., Samuels, B. L., Song, S. M., , Spelman, M. J., Stouer,
1112 R. J., Sweeney, C. O., Vecchi, G., Winton, M., Wittenberg, A. T., Zeng,
1113 F., Zhang, R., 2006: GFDL's CM2 global coupled climate models-Part
1114 2: The baseline ocean simulation. *J. Climate*, **19**, 675-697.

1115 Griffies, S. M., 2009: Elements of MOM4p1. Available at <http://www.gfdl.noaa.gov/fms>.

1116 —, A. Gnanadesikan, K.W. Dixon, J.P. Dunne, R. Gerdes, M.J. Harrison,
1117 A. Rosati, J. Russell, B.L. Samuels, M.J. Spelman, M. Winton, and R.
1118 Zhang, 2005: Formulation of an ocean model for global climate simula-

1119 tions. *Ocean Science*, **1**, 45-79.

1120 Griffies, S.M. J. Harrison, R. C. Pacanowski, and A. Rosati, 2004: A Tech-
1121 nical Guide to MOM4. Available at <http://www.gfdl.noaa.gov/fms>.

1122 Griffies, S.M., A. Biastoch, C. Boening, F. Bryan, E. Chassignet, M. Eng-
1123 land, R. Gerdes, H. Haak, R.W. Hallberg, W. Hazeleger, J. Jungclaus,
1124 W.G. Large, G. Madec, B.L. Samuels, M. Scheinert, A. Sen Gupta, C.A.
1125 Severijns, H.L. Simmons, A.-M. Treguier, M. Winton, S. Yeager, J. Yin,
1126 2009: Coordinated Ocean-ice Reference Experiments (COREs). *Ocean*
1127 *Modeling*, **26**, i-46

1128 Griffies, S.M., M. Winton, L.J. Donner, S.M. Downes, R. Farneti, A. Gnanade-
1129 sekin, L.W Horowitz, W.J. Hurlin, H.-C. Lee, J. B. Palter, B.L. Samuels,
1130 A.T. Wittenberg, B.L. Wyman, J. Yin, 2010: GFDL's CM3 coupled cli-
1131 mate model: Characteristics of the ocean and sea ice simulations. *J.*
1132 *Climate*, submitted.

1133 Guo, H., J.-C. Golaz, L.J. Donner, V.E. Larson, D.P. Schanen, and B.M.
1134 Griffin, 2010: A dynamic probability density function treatment of cloud
1135 mass and number concentrations for low level clouds in GFDL SCM/GCM.
1136 *Geosci. Model Dev. Discuss.*, **3**, 541-588.

1137 Hanson, D.R. and K. Mauersberger, 1988: Laboratory studies of nitric acid
1138 trihydrate: Implications for the south polar stratosphere. *Geophys. Res.*

1139 *Lett.*, **15**, 855-858.

1140 Harrison, E.F., P. Minnis, B.R. Barkstrom, V. Ramanathan, R.D. Cess, and
 1141 G.G. Gibson, 1990: Seasonal variation of cloud radiative forcing derived
 1142 from the Earth Radiation Budget Experiment. *J. Geophys. Res.*, **95**,
 1143 18,687-18,703.

1144 Haywood, J.M. and Ramaswamy, V., 1998: Global sensitivity studies of the
 1145 direct radiative forcing due to anthropogenic sulfate and black carbon
 1146 aerosols. *J. Geophys. Res.*, **103**, 6043-6058.

1147 Held, I.M., R.S. Hemler, and V. Ramaswamy, 1993: Radiative-convective
 1148 equilibrium with explicit two-dimensional moist convection. *J. Atmos.*
 1149 *Sci.*, **50**, 3909-3927.

1150 Hess, M., P. Koepke, and I. Schult, 1998: Optical properties of aerosols and
 1151 clouds: The software package OPAC. *Bull. Amer. Meteor. Soc.*, **79**,
 1152 831-844.

1153 Hess, P.G., S. Flocke, J.-F. Lamarque, M.C. Barth, and S. Madronich, 2000:
 1154 Episodic modeling of the chemical structure of the troposphere as re-
 1155 vealed during the spring MLOPEX 2 intensive. *J. Geophys. Res.*, **105**,
 1156 doi:10.1029/2000JD900253.

1157 Heymsfield, A.J., and L.J. Donner, 1990: A scheme for parameterizing ice-
 1158 cloud water content in general circulation models. *J. Atmos. Sci.*, **47**,

1159 1865-1877.

1160 Holben, B.N., T.F. Eck, I. Slutsker, D. Tanre, J.P. Buis, A. Setzer, E. Ver-
1161 mote, J.A. Reagan, Y.J. Kaufman, T. Nakajima, et al., 1998: AERONET—
1162 A federated instrument network and data archive for aerosol characteri-
1163 zation. *Remote Sensing of Environment*, **66**, 1-16.

1164 Holtslag, A. A. M., and B.A. Boville, 1993: Local versus nonlocal boundary-
1165 layer diffusion in a global climate model. *J. Climate*, **6**, 1825-1842.

1166 Horowitz, L.W., 2006: Past, present, and future concentrations of tropo-
1167 spheric ozone and aerosols: Methodology, ozone evaluation, and sensitiv-
1168 ity to aerosol wet removal. *J. Geophys. Res.*, **111**, doi:10.1029/2005JD006937.

1169 Horowitz, L.W., S. Walters, D. Mauzerall, L.K. Emmons. P.J. Rasch, C.
1170 Granier, X. Tie, J.-F. Lamarque, M.G. Schultz, G.S. Tyndall, J.J. Or-
1171 lando, and G.P. Brasseur, 2003: A global simulation of tropospheric
1172 ozone and related tracers: description and evaluation of MOZART, ver-
1173 sion 2. *J. Geophys. Res.*, **108**, D24, doi:10.1029/2002JD002853.

1174 Huffman, G.J., R.F. Adler, P.A. Arkin, A. Chang, R. Ferraro, A. Gruber, J.
1175 Janowiak, R.J. Joyce, A. McNab, B. Rudolf, U. Schneider, and P. Xie,
1176 1997: The global precipitation climatology project (GPCP) combined
1177 precipitation data set. *Bull. Amer. Meteor. Soc.*, **78**, 5-20.

1178 Hurrell, J., J. Hack, D. Shea, J. Caron, and J. Rosinski, 2008: A new sea

1179 surface temperature and sea ice boundary data set for the Community
1180 Atmosphere Model. *J. Climate*, **21**, 2428-2446.

1181 Kalnay, E., and Co-authors, 1996: The NCEP/NCAR 40-year re-analysis
1182 project. *Bull. Amer. Meteor. Soc.*, **77**, 437-471.

1183 King, M. D., W. P. Menzel, Y. J. Kaufman, D. Tanre, B.-C. Gao, S. Plat-
1184 nick, S. A. Ackerman, L. A. Remer, R. Pincus, and P. A. Hubanks, 2003:
1185 Cloud and aerosol properties, precipitable water, and profiles of temper-
1186 ature and humidity. *IEEE Trans. Geosci. Remote Sens.*, **41**, 442-458,
1187 doi:10.1109/TGRS.2002.808226.

1188 Knutson, T.R., T.L. Delworth, K.W. Dixon, I.M. Held, J. Lu, V. Ramaswamy,
1189 M.D. Schwarzkopf, G. Stenchikov, and R.J. Stouffer, 2006: Assessment of
1190 twentieth-century regional surface trends using the GFDL CM2 coupled
1191 models. *J. Climate*, **19**, 1624-1651.

1192 Kopp, G., Lawrence, G., and Rottman, G., 2005: The Total Irradiance Mon-
1193 itor (TIM): Science Results. *Solar Physics*, **230**, 129-140.

1194 Lamarque, J.-F., T.C. Bond, V. Eyring, C. Granier, A. Heil, Z. Klimont,
1195 D. Lee, C. Liou, A. Mieville, B. Owen, M.G. Schultz, D. Shindell,
1196 S.J. Smith, E. Stehfest, J. Van Aardenne, O.R. Cooper, M. Kainuma,
1197 N. Mahowald, J.R. McConnell, V. Naik, K. Riahi, and D.P. van Vuuren,
1198 2010: Historical (1850-2000) gridded anthropogenic and biomass burning

1199 emissions of reactive gases and aerosols: Methodology and application.
1200 *Atmos. Chem. Phys. Discuss.*, **10**, 4963-5019.

1201 Large, W.G., and S.G. Yeager, 2009: The global climatology of an interan-
1202 nually varying air-sea flux data set. *Clim. Dyn.*, **33**, 341-364.

1203 Leary, C.A., and R.A. Houze, Jr., 1980: The contribution of mesoscale mo-
1204 tions to the mass and heat fluxes of an intense tropical convective system.
1205 *J. Atmos. Sci.*, **37**, 784-796.

1206 Li, F., P. Ginoux, and V. Ramaswamy, 2008: Distribution, transport, and de-
1207 position of mineral dust in the Southern Ocean and Antarctica: Contribu-
1208 tion of major sources. *J. Geophys. Res.*, **113**, doi:10.1029/2007JD009190.

1209 Liao, H. and J.H. Seinfeld, 2005: Global impacts of gas-phase chemistry-
1210 aerosol interactions on direct radiative forcing by anthropogenic aerosols
1211 and ozone. *J. Geophys. Res.*, **110**, doi:10.1029/2005JD005.

1212 Liebmann, B., and C. A. Smith, 1996: Description of a complete (interpo-
1213 lated) outgoing longwave radiation dataset. *Bull. Amer. Meteor. Soc.*,
1214 **77**, 1275-1277.

1215 Lin, J.-L., G.N. Kiladis, B.E. Mapes, K.M. Weickmann, K.R. Sperber, W.
1216 Lin, M. Wheeler, S.D. Schubert, A. Del Genio, L.J. Donner, S. Emori,
1217 J.-F. Gueremy, F. Hourdin, P.J. Rasch, E. Roeckner, and J.F. Scinocca,
1218 2006: Tropical intraseasonal variability in 14 IPCC AR4 climate models.

- 1219 Part I. Convective signals. *J. Climate*, **19**, 2665-2690.
- 1220 Lin, S.-J., 1997: A finite-volume integration method for computing pressure-
 1221 gradient force in general vertical coordinates. *Quart. J. Roy. Meteor.*
 1222 *Soc.*, **123**, 1749-1762.
- 1223 —, 2004: A “vertically Lagrangian” finite-volume dynamical core for global
 1224 models. *Mon. Wea. Rev.*, **132**, 2293-2307.
- 1225 —, and R. B. Rood, 1996: Multidimensional flux-form semi-lagrangian
 1226 transport schemes. *Mon. Wea. Rev.* **124**, 2046-2070.
- 1227 —, 1997: An explicit flux-form semi-Lagrangian shallow water model on
 1228 the sphere. *Quart. J. Roy. Meteor. Soc.*, **123**, 2477-2498.
- 1229 Lock, A.P., A.R. Brown, M.R. Bush, M. Martin, and R.N.B. Smith, 2000:
 1230 A new boundary layer mixing scheme. Part I: Scheme description and
 1231 single-column model tests. *Mon. Wea. Rev.*, **128**, 3187-3199.
- 1232 Loeb, N., B.A. Wielicki, D.R. Doelling, G.L. Smith, D.F. Keyes, S. Kato,
 1233 N. Manalo-Smith, and T. Wong, 2009: Toward optimal closure of the
 1234 earth’s top-of-atmosphere radiation budget. *J. Climate*, **22**, 748-766.
- 1235 Louis, J.-F., 1979: A parametric model of vertical eddy fluxes in the atmo-
 1236 sphere. *Bound.-Layer Meteor.*, **17**, 187-202.
- 1237 Madronich, S. and S. Flocke, 1998: The role of solar radiation in atmo-

1238 spheric chemistry. *Handbook of Environmental Chemistry*, P. Boule, ed.,
1239 Springer-Verlag, Heidelberg, pp. 1-26.

1240 Manabe, S., J. Smagorinsky, and R.F. Strickler, 1965: Simulated climatology
1241 of a general circulation model with hydrologic cycle. *Mon. Wea. Rev.*,
1242 **93**, 769-798.

1243 McFarquhar, G.M., A.J. Heymsfield, A. Macke, J. Iaquinta, and S.M. Aulen-
1244 bach, 1999: Use of observed ice crystal sizes and shapes to calculate mean
1245 scattering properties and multi-spectral radiances: CEPEX April 4, 1993
1246 case study. *J. Geophys. Res.*, **104**(D24), 31,763-31,780.

1247 Meehl, G. A., C. Covey, T. Delworth, M. Latif, B. McAvaney, J. F. B.
1248 Mitchell, R. J. Stouffer, and K. E. Taylor, 2007: The WCRP CMIP3
1249 multi-model dataset: A new era in climate change research. *Bull. Amer.*
1250 *Meteor. Soc.* **88**, 1383-1394.

1251 Milly, P.C.D., and A.B. Shmakin, 2002: Global modeling of land water and
1252 energy balances. Part I: The land dynamics (LaD) model. *J. Hydrome-*
1253 *teorology*, **3**, 283-299.

1254 Ming, Y., and L.M. Russell, 2004: Organic aerosol effects on fog droplet
1255 spectra. *J. Geophys. Res.*, **109**, doi:10.1029/2003JD004.

1256 Ming, Y., V. Ramaswamy, L.J. Donner, and V.T.J. Phillips, 2006: A robust
1257 parameterization of cloud droplet activation. *J. Atmos. Sci.*, **63**, 1348-

1258 1356.

1259 Ming, Y., V. Ramaswamy, P.A. Ginoux, and L.W. Horowitz, 2005: Direct
 1260 radiative forcing of anthropogenic organic aerosols. *J. Geophys. Res.*,
 1261 **110**, doi:10.1029/2004JD0005.

1262 Monahan, E. C., D. E. Spiel, and K. L. Davidson, 1986: A model of marine
 1263 aerosol generation via whitecaps and wave disruption. *Oceanic White-*
 1264 *caps*, E. C. Monahan and G. Mac Niocaill, Eds., D. Reidel, 167-174.

1265 O'Dowd, C.D., B. Langmann, S. Varghese, C. Scannell, D. Ceburnis, and
 1266 M.C. Facchini, 2008: A combined organic-inorganic sea-spray source
 1267 function. *Geophys. Res. Lett.*, **35**, doi:10.1029/2007GL030331.

1268 Perovich, D., T. C. Grenfell, B. Light, and P. V. Hobbs, 2002: Seasonal
 1269 evolution of the albedo of multi-year arctic sea ice. *J. Geophys. Res.*,
 1270 **107**, doi:10.1029/2000JC000438.

1271 Pincus, R., H. W. Barker, and J. Morcrette, 2003: A fast, flexible, approxi-
 1272 mate technique for computing radiative transfer in inhomogeneous cloud
 1273 fields. *J. Geophys. Res.*, **108(D13)**, 4376, doi:10.1029/2002JD003322.

1274 Pincus, R., C. P. Batstone, R. J. P. Hofmann, K. E. Taylor, and P. J.
 1275 Glecker, 2008: Evaluating the present-day simulation of clouds, pre-
 1276 cipitation, and radiation in climate models. *J. Geophys. Res.*, **113**,
 1277 doi:10.1029/2007JD009334.

- 1278 Pincus, R., C. Hannay, S. A. Klein, K.-M. Xu, and R. Hemler, 2005: Overlap
1279 assumptions for assumed probability distribution function cloud schemes
1280 in large-scale models. *J. Geophys. Res.*, **110**, D15S09, doi:10.1029/2004JD005100.
- 1281 Pincus, R., R. Hemler, and S.A. Klein, 2006: Using stochastically generated
1282 sub-columns to represent cloud structure in a large-scale model. *Mon.*
1283 *Wea. Rev.*, **134**, 3644-3656. doi:10.1175/MWR3257.1.
- 1284 Putman, W. M. and S.-J. Lin, 2007: Finite-volume transport on various
1285 cubed-sphere grid. *J. Comput. Phys.*, **227**, 5578.
- 1286 Randel, W.J. and F. Wu, 2007: A stratospheric ozone profile data set for
1287 1979-2005: Variability, trends, and comparisons with column ozone data.
1288 *J. Geophys. Res.*, **112**, doi:10.1029/2006JD007339.
- 1289 Rayner, N.A., D.E. Parker, E.B. Horton, C.K. Folland, L.V. Alexander, and
1290 D.P. Rowell, 2003: Global analyses of sea surface temperature, sea ice,
1291 and night marine air temperature since the late nineteenth century. *J.*
1292 *Geophys. Res.*, **108**, doi:10.1029/2002JD002670.
- 1293 Reichler, T., and J. Kim, 2008: How well do coupled models simulate today's
1294 climate? *Bull. Amer. Meteor. Soc.*, **89**, 303-311.
- 1295 Rotstayn, L.D., 1997: A physically based scheme for the treatment of strat-
1296 iform clouds and precipitation in large-scale models. I: Description and
1297 evaluation of microphysical processes. *Quart. J. Roy. Meteor. Soc.*,

1298 **123**, 1227-1282.

1299 —, B.F. Ryan, and J. Katzfey, 2000: A scheme for calculation of the liquid
1300 fraction in mixed-phase clouds in large-scale models. *Mon. Wea. Rev.*,
1301 **128**, 1070-1088.

1302 Sadourny, R. 1972: Conservative finite-difference approximations of the prim-
1303 itive equations on quasi-uniform spherical grids. *Mon. Wea. Rev.*, **144**,
1304 136-144.

1305 Sander, S.P., R.R. Friedl, D.M. Golden, M.J. Kurylo, R.E. Huie, V.L. Orkin,
1306 G.K. Moortgat, A.R. Ravishankara, C.E. Kolb, M.J. Molina, B.J. Finlayson-
1307 Pitts, 2006: Chemical kinetics and photochemical data for use in atmo-
1308 spheric studies. Evaluation No. 15, JPL Publication 06-2, Jet Propulsion
1309 Laboratory, Pasadena, CA, USA.

1310 Schwarzkopf, M.D., and V. Ramaswamy, 1999: Radiative effects of CH₄,
1311 N₂O, halocarbons and the foreign-broadened H₂O continuum: A GCM
1312 experiment. *J. Geophys. Res.*, **104**, 9467-9488.

1313 Shevliakova, E., S.W. Pacala, S. Malyshev, G.C. Hurtt, P.C.D. Milly, J.D.
1314 Caspersen, L.T. Sentman, J.P. Fisk, C. Wirth, C. Crevoisier, 2009: Car-
1315 bon cycling under 300 years of land use change: Importance of the
1316 secondary vegetation sink. *Global Biogeochemical Cycles*, **23**, GB2022,
1317 doi:10.1029/2007GB003176.

- 1318 Simmons, A.J., and D.M. Burridge, 1981: An energy and angular-momentum
1319 conserving vertical finite-difference scheme and hybrid vertical coordi-
1320 nates. *Mon. Wea. Rev.*, **109**, 758-766.
- 1321 Slingo, A., 1989: A GCM parameterization for the shortwave radiative prop-
1322 erties of water clouds. *J. Atmos. Sci.*, **46**, 1419-1427.
- 1323 Stenchikov, G., K. Hamilton, R. J. Stouffer, A. Robock, V. Ramaswamy,
1324 B. Santer, and H.-F. Graf, 2006: Arctic Oscillation response to volcanic
1325 eruptions in the IPCC AR4 climate models. *J. Geophys. Res.*, **111**,
1326 D07107, doi:10.1029/2005JD006286.
- 1327 Stern, W.F., and R.T. Pierrehumbert, 1988: The impact of an orographic
1328 gravity wave drag parameterization on extended-range predictions with
1329 a GCM. *Preprints, Eighth Conf. on Numerical Weather Prediction*, Bal-
1330 timore, MD, Amer. Meteor. Soc., 745-750.
- 1331 Stolarski, R. S., and S. Frith, 2006: Search for evidence of trend slowdown
1332 in the long-term TOMS/SBUV total ozone data record: The importance
1333 of instrument drift uncertainty. *Atmos. Chem. Phys.*, **12**, 4057-4065.
- 1334 Tang, I.N., and H.R. Munkelwitz, 1994: Water activities, densities, and re-
1335 fractive indices of aqueous sulfates and sodium nitrate droplets of atmo-
1336 spheric importance. *J. Geophys. Res.*, **99**, 18801-18808.
- 1337 Tang, I. N., A. C. Tridico, and K. H. Fung, 1997: Thermodynamic and optical

1338 properties of sea-salt aerosols. *J. Geophys. Res.*, **102**, 23269-23276.

1339 Taylor, K.E., 2001: Summarizing multiple aspects of model performance in
1340 a single diagram. *J. Geophys. Res.*, **106**, 7183-7192.

1341 Thompson, D.W.J., and S. Solomon, 2006: Interpretation of recent Southern
1342 Hemisphere climate change. *Science*, **296**, 895-899.

1343 Tie, X., S. Madronich, S. Walters, D. P. Edwards, P. Ginoux, N. Mahowald,
1344 R. Zhang, C. Lou, and G. Brasseur, 2005: Assessment of the global
1345 impact of aerosols on tropospheric oxidants. *J. Geophys. Res.*, **110**,
1346 doi:10.1029/2004JD005359.

1347 Tiedtke, M., 1993: Representation of clouds in large-scale models. *Mon.*
1348 *Wea. Rev.*, **121**, 3030-3061.

1349 Trenberth, K.E., and J.M. Caron, 2001: Estimates of meridional atmosphere
1350 and ocean heat transports. *J. Climate*, **14**, 3433-3443.

1351 Uppala, S.M., Kålberg, P.W., Simmons, A.J., Andrae, U., da Costa Bech-
1352 told, V., Fiorino, M., Gibson, J.K., Haseler, J., Hernandez, A., Kelly,
1353 G.A., Li, X., Onogi, K., Saarinen, S., Sokka, N., Allan, R.P., Andersson,
1354 E., Arpe, K., Balmaseda, M.A., Beljaars, A.C.M., van de Berg, L., Bid-
1355 lot, J., Bormann, N., Caires, S., Chevallier, F., Dethof, A., Dragosavac,
1356 M., Fisher, M., Fuentes, M., Hagemann, S., Hólm, E., Hoskins, B.J.,
1357 Isaksen, I., Janssen, P.A.E.M., Jenne, R., McNally, A.P., Mahfouf, J.-

1358 F., Morcrette, J.-J., Rayner, N.A., Saunders, R.W., Simon, P., Sterl,
1359 A., Trenberth, K.E., Untch, A., Vasiljevic, D., Viterbo, P., and Woollen,
1360 J. 2005: The ERA-40 re-analysis. *Quart. J. R. Meteorol. Soc.*, **131**,
1361 2961-3012, doi:10.1256/qj.04.176.

1362 Vitart, F., J.L. Anderson, and W.F. Stern, 1997: Simulation of interannual
1363 variability of tropical storm frequency in an ensemble of of GCM inte-
1364 grations. *Mon. Wea. Rev.*, **129**, 2521-2537.

1365 Wesely, M.L., 1989: Parameterization of surface resistance to gaseous dry
1366 deposition in regional-scale numerical models. *Atmos. Environ.*, **23**,
1367 1293-1304.

1368 Wheeler, M., and G.N. Kiladis, 1999: Convectively coupled equatorial waves.
1369 Analysis of clouds and temperature in the wavenumber-frequency do-
1370 main. *J. Atmos. Sci.*, **56**, 374-399.

1371 Wielicki, B.A., B.R. Barkstrom, E.F. Harrison, R.B. Lee III, G.L. Smith,
1372 and J.E. Cooper, 1996: Clouds and the Earth's Radiant Energy System
1373 (CERES): An earth observing system experiment. *Bull. Amer. Meteor.*
1374 *Soc.*, **77**, 853-868.

1375 Wilcox, E.M., and L.J. Donner, 2007: The frequency of extreme rain events
1376 in satellite rain-rate estimates and an atmospheric general circulation
1377 model. *J. Climate*, **20**, 53-69.

- 1378 Winton, M., 2000: A reformulated three-layer sea ice model. *J. Atmos.*
1379 *Ocean. Technol.*, **17**, 525-531.
- 1380 Woodruff, S.D., R.J. Slutz, R.L. Jenne, and P.M. Steurer, 1987: A Compre-
1381 hensive Ocean-Atmosphere Dataset. *Bull. Amer. Meteor. Soc.*, **68**,
1382 1239.
- 1383 Zhang, G., 2002: Convective quasi-equilibrium in mid-latitude continental
1384 environment and its effect on convective parameterization. *J. Geophys.*
1385 *Res.*, **107**, doi: 10.1029/2001JD001005.
- 1386 —, 2009: Effects on entrainment on convective available potential energy
1387 and closure assumptions in convection parameterization. *J. Geophys.*
1388 *Res.*, **114**, doi:10.1029/2008JD10976.
- 1389 Zhang, X., W. Lin, and M. Zhang, 2007: Toward understanding the double
1390 Inter-tropical Convergence Zone pathology in coupled ocean-atmosphere
1391 general circulation models. *J. Geophys. Res.*, **112**, doi:10.1029/2006JD007878.
- 1392 Zhao, M., I.M. Held, S-J. Lin, and G.A. Vecchi, 2009: Simulations of global
1393 hurricane climatology, interannual variability, and response to global
1394 warming using a 50km resolution GCM. *J. Climate*, **22**, 6653-6678.

FIGURE LEGENDS

1395 Fig. 1. AM3 annual-mean, zonally averaged cumulus mass fluxes for (a) all
1396 convection (except MAA), (b) cell updrafts, (c) mesoscale updrafts, (d)
1397 mesoscale downdrafts, and (e) shallow cumulus.

1398 Fig. 2. Annual-mean, zonally averaged precipitation for (a) AM3 and (b)
1399 CM3.

1400 Fig. 3. Climatological aerosol optical depths (550nm) from AERONET and
1401 (a), (b) CM2.1 and (c), (d) CM3. Dashed lines in (a) and (c) denote
1402 slopes of 0.5 and 2.

1403 Fig. 4. Climatological aerosol co-albedos from AERONET (440nm) and (a),
1404 (b) CM2.1 and (c), (d) CM3 (550nm). Dashed lines in (a) and (c) denote
1405 slopes of 0.5 and 2.

1406 Fig. 5. Surface clear-sky downward shortwave fluxes from BSRN and (a)
1407 CM2.1 and (c) CM3. Differences in these fluxes: (b) CM2.1 minus BSRN
1408 and (d) CM3 minus BSRN.

1409 Fig. 6. Cloud-drop radius from MODIS simulator in AM3 for (a) January
1410 and (b) July. Cloud-drop radius from MODIS for (c) January and (d)
1411 July.

1412 Fig. 7. Annual-mean, zonally averaged ozone from (a) AM3 and (b) TOMS.

1413 Fig. 8. Vertically integrated, zonally averaged ozone for 1980-1989 from
1414 (a) TOMS, (b) AM3 and for 1990-1999 from (c) TOMS, (d) AM3. (e)
1415 Annual-mean difference between AM3 and TOMS vertically integrated,
1416 zonally averaged ozone.

1417 Fig. 9. Annual-mean shortwave absorbed radiation for (a) AM3, (b) ERBE,
1418 (c) AM3 minus ERBE, and (d) CM3 minus ERBE.

1419 Fig. 10. Annual-mean outgoing longwave radiation for (a) AM3, (b) ERBE,
1420 (c) AM3 minus ERBE, and (d) CM3 minus ERBE.

1421 Fig. 11. Taylor diagrams for top-of-atmosphere (TOA) radiation balance.
1422 The root-mean-square (RMS) errors, correlations, and standard devia-
1423 tions are based on global, annual means.

1424 Fig. 12. January 2007 cloud fractions from (a) AM3 CALIPSO simulator
1425 and (b) CALIPSO.

1426 Fig. 13. Implied ocean heat transport for (a) total ocean, (b) Atlantic Ocean,
1427 and (c) Indo-Pacific Ocean. Dashed lines and vertical bars indicate range
1428 of one standard error above and below Trenberth and Caron (2001) and
1429 Ganachaud and Wunsch (2003) estimates, respectively.

1430 Fig. 14. Annual-mean, zonally averaged zonal wind for (a) AM3, (b) ERA-
1431 40, (c) AM3 minus ERA-40, and (d) CM3 minus ERA-40.

1432 Fig. 15. Annual-mean wind stress for (a) Pacific Ocean and (b) Atlantic
1433 Ocean.

1434 Fig. 16. Northern Hemisphere DJF sea-level pressure minus 1013.25 hPa for
1435 (a) AM3, (b) NCEP re-analysis, (c) AM3 minus NCEP re-analysis, and
1436 (d) CM3 minus NCEP re-analysis. Contour intervals: (a), (b) 3 hPa; (c)
1437 1 hPa. Areas with mean surface pressures less than 950 hPa are masked.

1438 Fig. 17. DJF departure from zonally averaged 500-hPa geopotential height
1439 for (a) AM3, (b) NCEP re-analysis, (c) AM3 minus NCEP re-analysis,
1440 and (d) CM3 minus NCEP re-analysis.

1441 Fig. 18. DJF product of the standard deviation of the Niño-3 index and re-
1442 gression coefficient between precipitation and Niño-3 index for (a) AM3,
1443 (b) CM3, and (c) GPCP.

1444 Fig. 19. Product of the standard deviation of the NAM index and regression
1445 coefficients between the NAM index and SLP (contours, hPa) and 2-m
1446 temperature (shading, $^{\circ}\text{C}$) for (a) AM3 and (b) NCEP re-analysis.

1447 Fig. 20. Tropical-cyclone frequency for (a) AM3, (b) CM3, (c) U.S. National
1448 Hurricane Center and Navy observations.

1449 Fig. 21. Normalized tropical symmetric OLR wavenumber-frequency power
1450 spectrum for (a) AM3, (b) AM3 with CAPE relaxation closure for deep
1451 cumulus replaced by a closure in which CAPE tendencies in the envi-

1452 ronment of cumulus parcels are balanced by deep convection with low-
 1453 level-lift trigger, and (c) OLR observations. Contour interval is .1 with
 1454 colored shading of regions greater than 1.2 indicating power associated
 1455 with MJO, Kelvin and other tropical convective waves that are signifi-
 1456 cantly above an approximately red-noise background power spectra. The
 1457 colored lines represent various equatorial wave dispersion curves labeled
 1458 for five different equivalent depths, i.e., 8, 12, 25, 50 and 90m.

1459 Fig. 22. Annual-mean, zonally averaged temperature for (a) AM3, (b) ERA-
 1460 40 re-analysis, (c) AM3 minus ERA-40, and (d) CM3 minus ERA-40.

1461 Fig. 23. Sea-surface temperatures for (a) CM3, (b) observations compiled at
 1462 Lawrence Livermore National Laboratory ([http://www-pcmdi.llnl.gov/projects/amip/](http://www-pcmdi.llnl.gov/projects/amip/AMIP2EXPDSN/BCS_OBS/amip2_bcs.htm)
 1463 [AMIP2EXPDSN/BCS_OBS/amip2_bcs.htm](http://www-pcmdi.llnl.gov/projects/amip/AMIP2EXPDSN/BCS_OBS/amip2_bcs.htm)), and (c) difference.

1464 Fig. 24. 2-m temperatures for (a) AM3, (b) CRU, (c) AM3 minus CRU, and
 1465 (d) CM3 minus CRU.

1466 Fig. 25. Annual-mean precipitation for (a) AM3, (b) GPCP v. 2, (c) AM3
 1467 minus GPCP v. 2, and (d) CM3 minus GPCP v. 2.

1468 Fig. 26. Precipitation intensity distribution from SSM/I and TMI, AM3, and
 1469 AM3 with CAPE relaxation closure for deep cumulus replaced by a clo-
 1470 sure in which CAPE tendencies in the environment of cumulus parcels are
 1471 balanced by deep convection with low-level-lift trigger. Shading brackets

1472 precipitation estimates from the SSM/I and TMI at $\pm 25\%$ bias.

1473 Fig. 27. Taylor diagrams for sea-level pressure, surface temperature, pre-
1474 cipitation, zonal surface wind stress, 200 hPa deviation of geopotential
1475 height from zonal mean, and 200 hPa zonal wind. Regions and peri-
1476 ods for averages as indicated. The ECHAM5-MPI, UKMO_HadGEM1,
1477 and NCAR-CCSM3 results are their latest AMIP submissions to the
1478 World Climate Research Program's CMIP3. Observations of sea-level
1479 pressure, geopotential height, and winds from NCEP re-analysis; precip-
1480 itation from GPCP v. 2; surface temperature from CRU; and wind stress
1481 from ERA-40.

1482 Fig. A1. Annual-mean sea-ice extent for (a) CM3, (b) observations, and
1483 (c) difference. Sea-ice extent is defined to be 1 if sea-ice concentration
1484 is 15% or greater and 0 otherwise. Observed ice extent is computed
1485 from monthly ice concentrations following Hurrell et al. (2008). Values
1486 between 0 and 1 result from time averaging.

Fig. 1

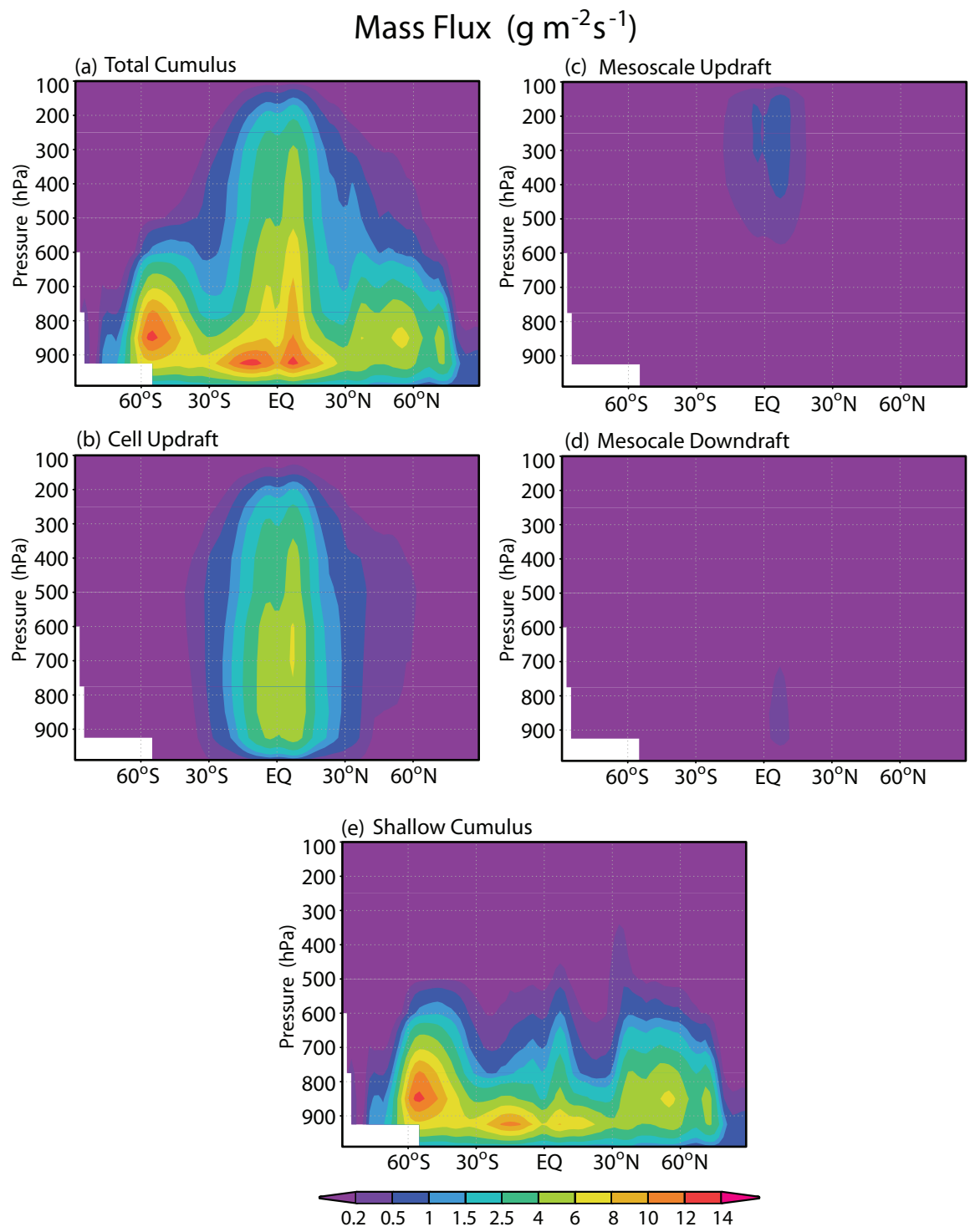


Fig. 2

Annual Precipitation

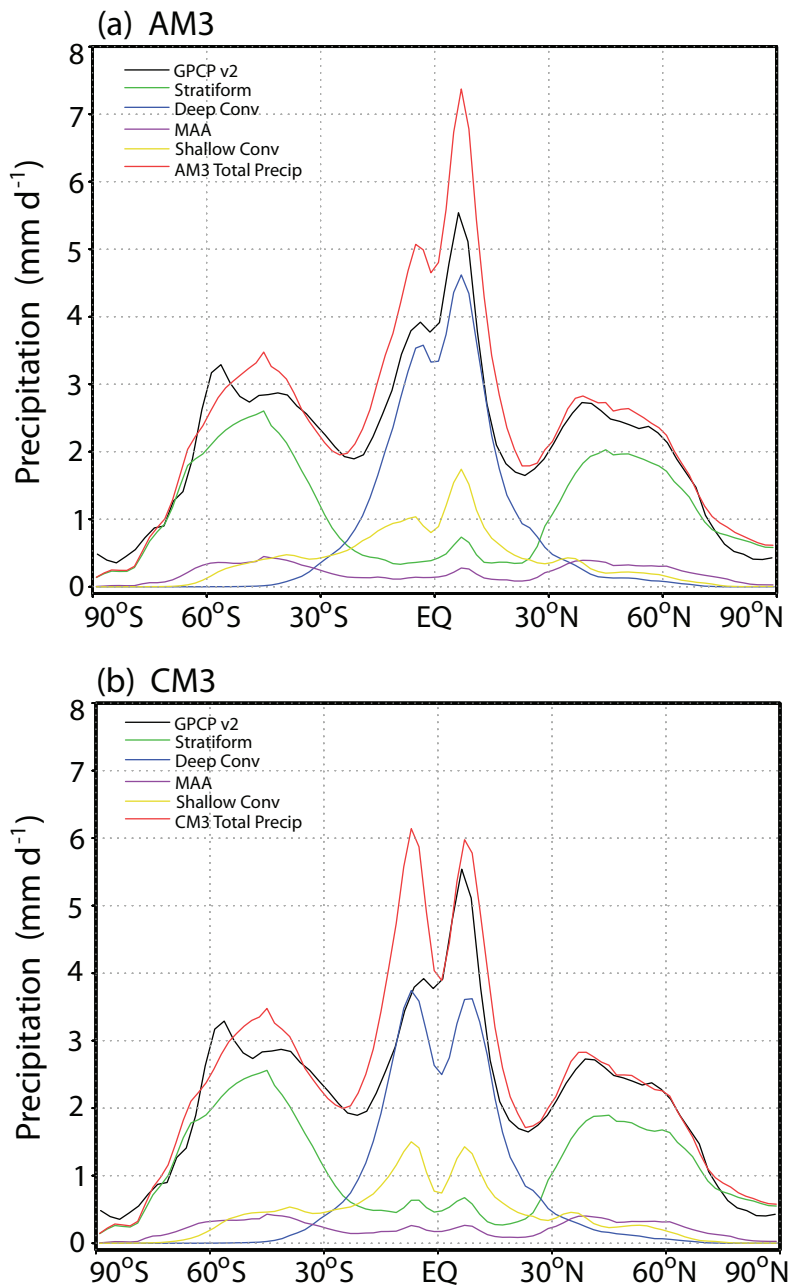


Fig. 3

Aerosol Optical Depth

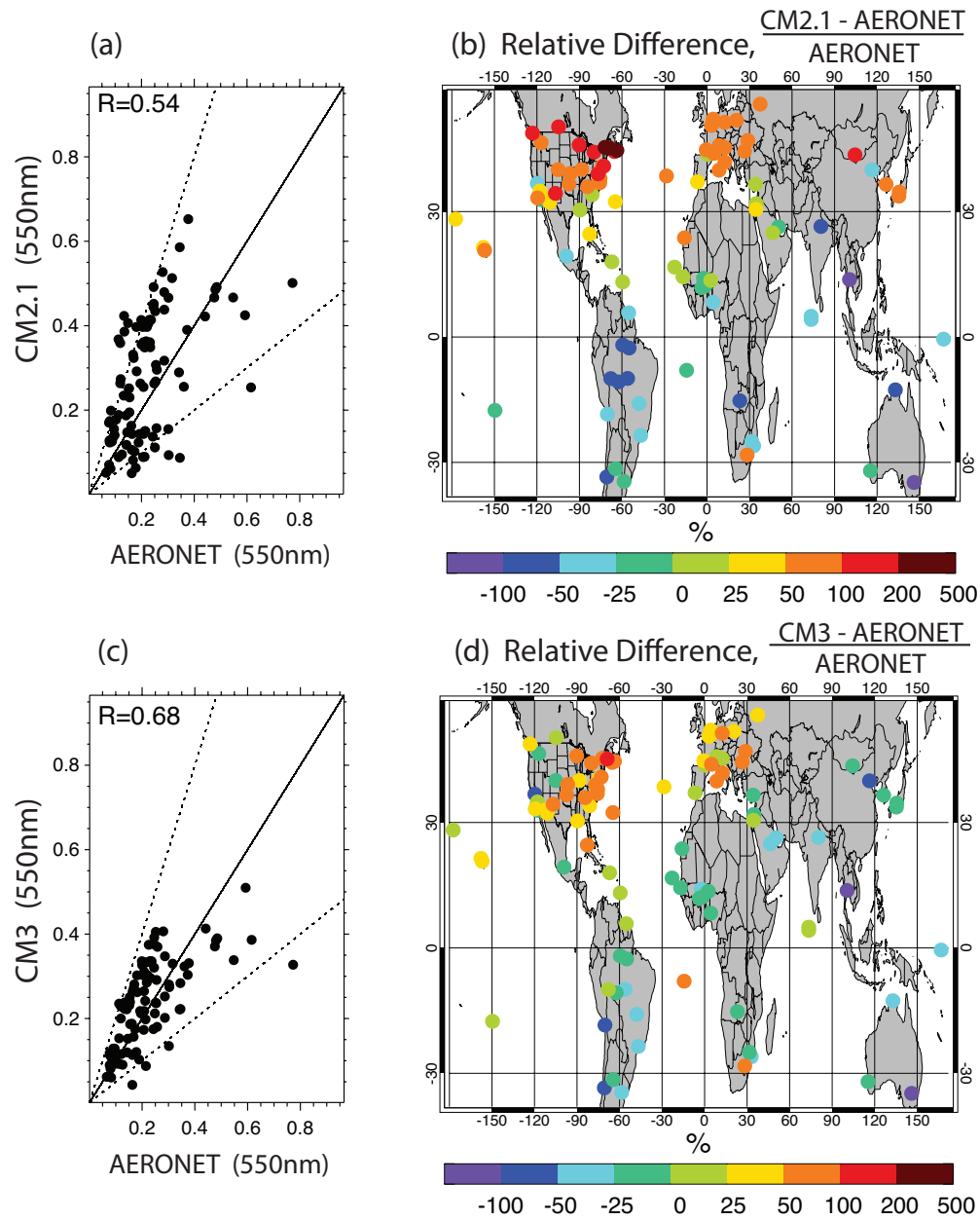


Fig. 4

Aerosol Co-albedo

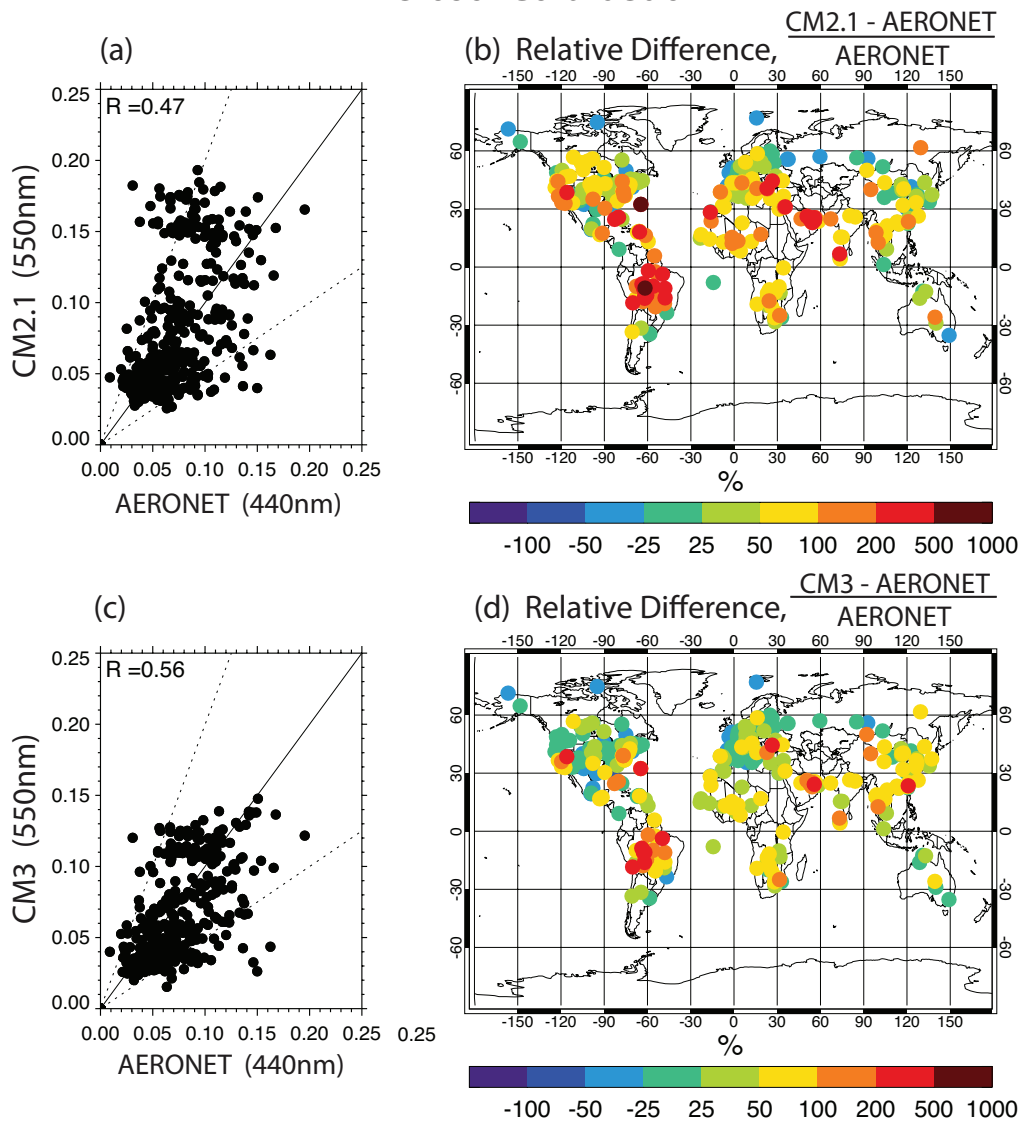


Fig. 5

Surface Clear-Sky Downward Shortwave Radiation

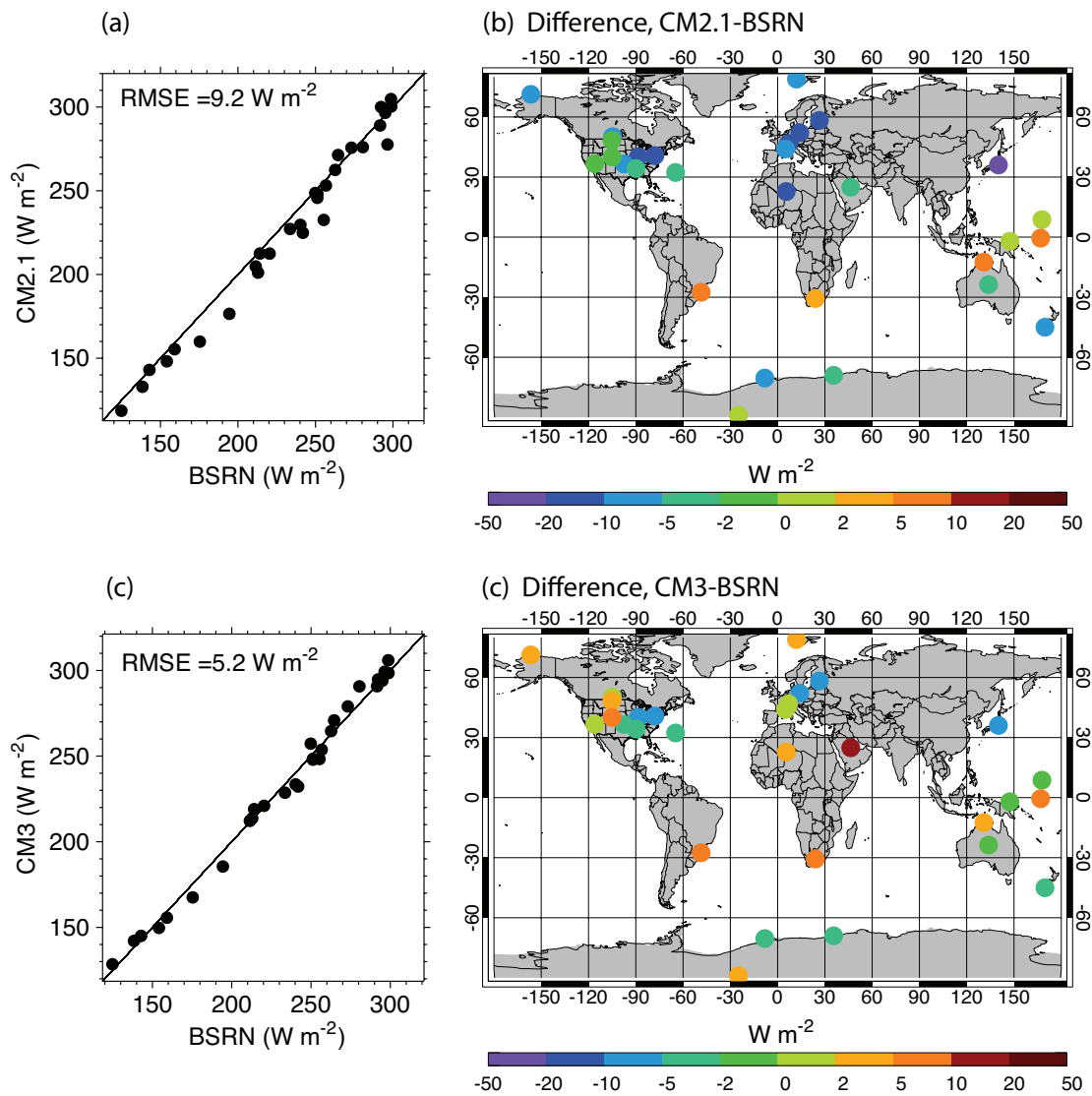


Fig. 6

Cloud - Drop Radius (μm)

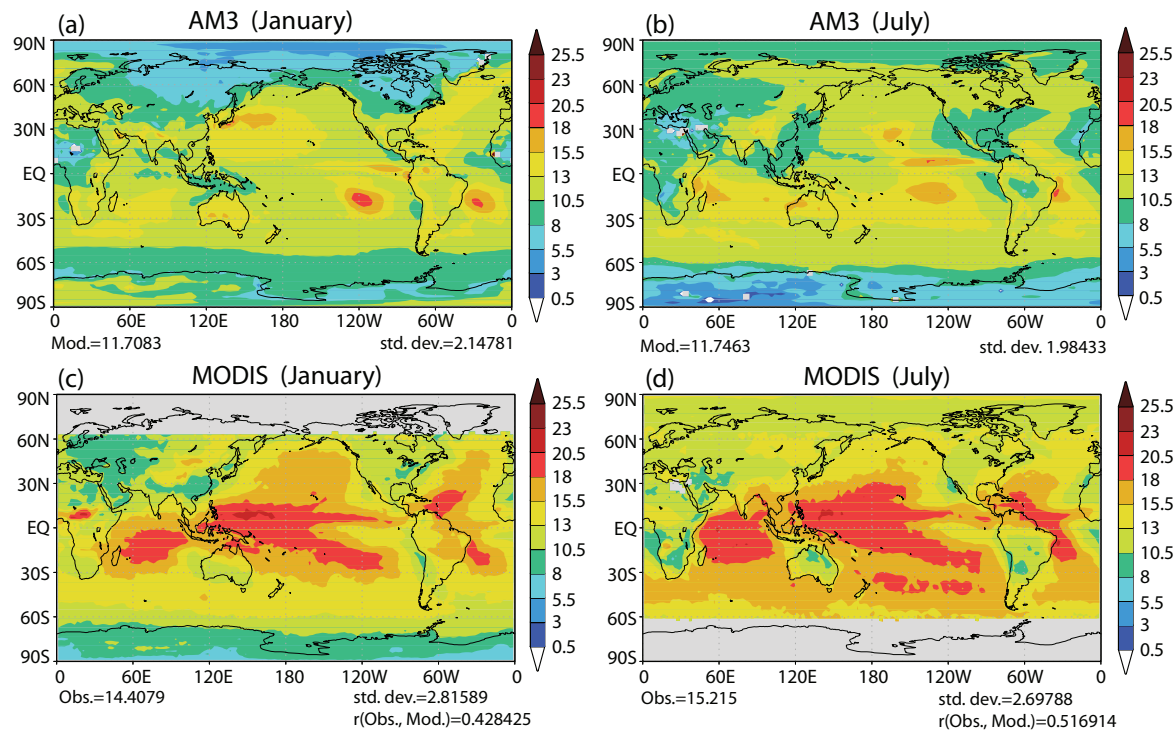


Fig. 7

Annual-Mean Ozone (ppmv)

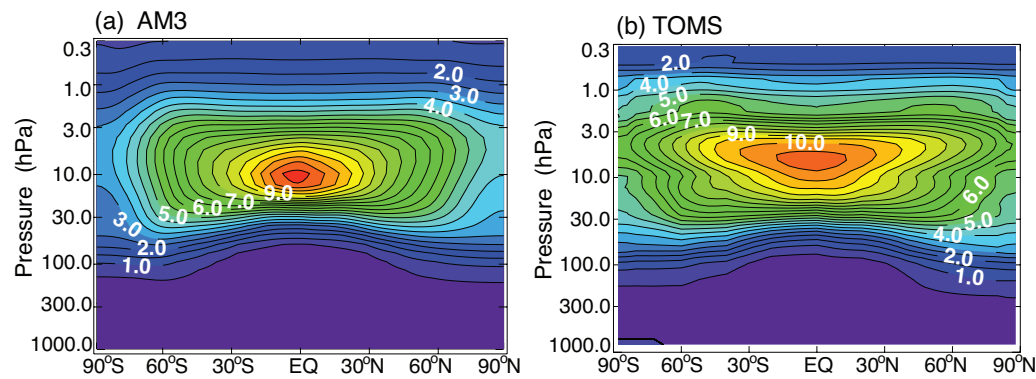


Fig. 8

Total Ozone (Dobson Units)

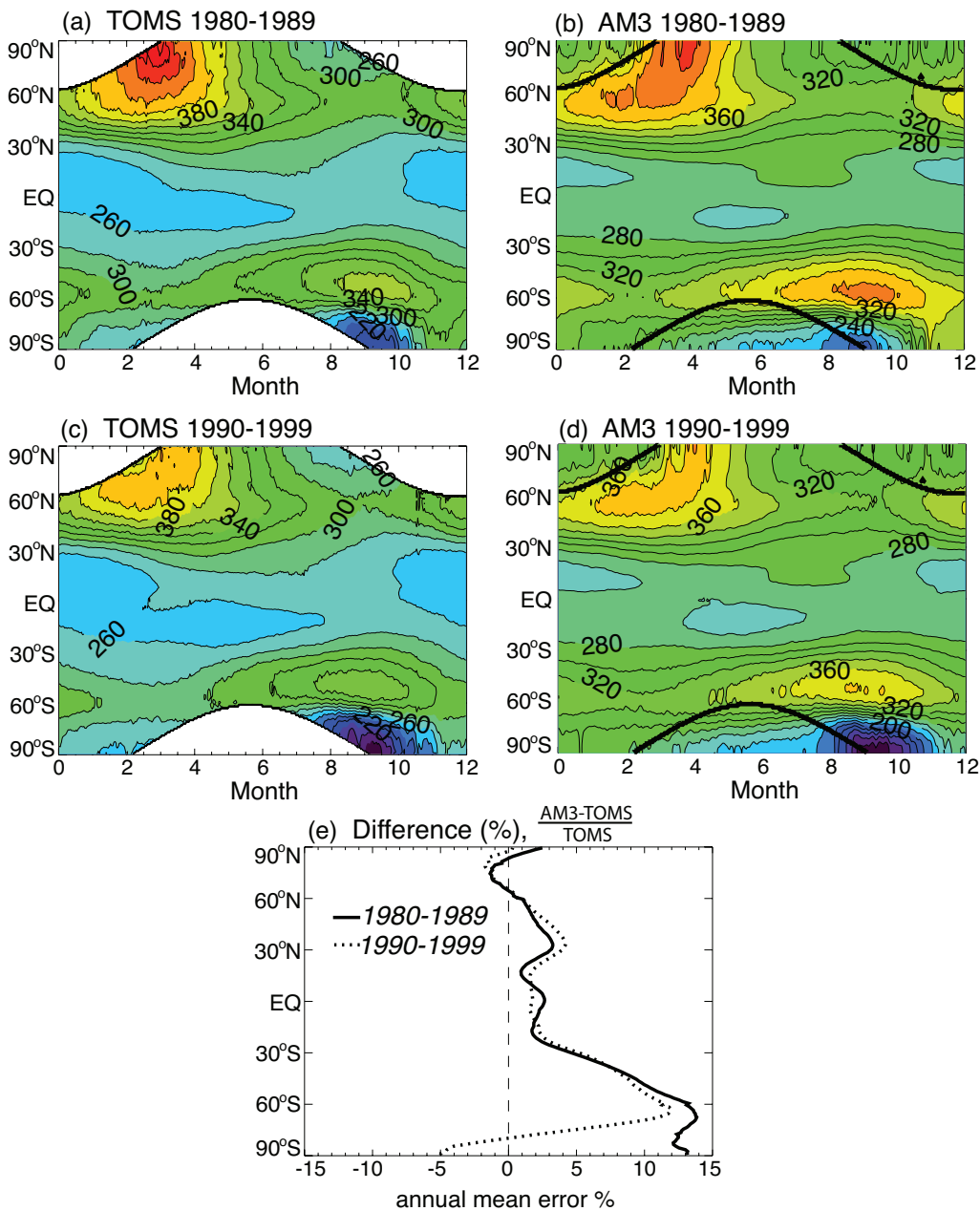


Fig. 9

Absorbed Shortwave Radiation (W/m^2)

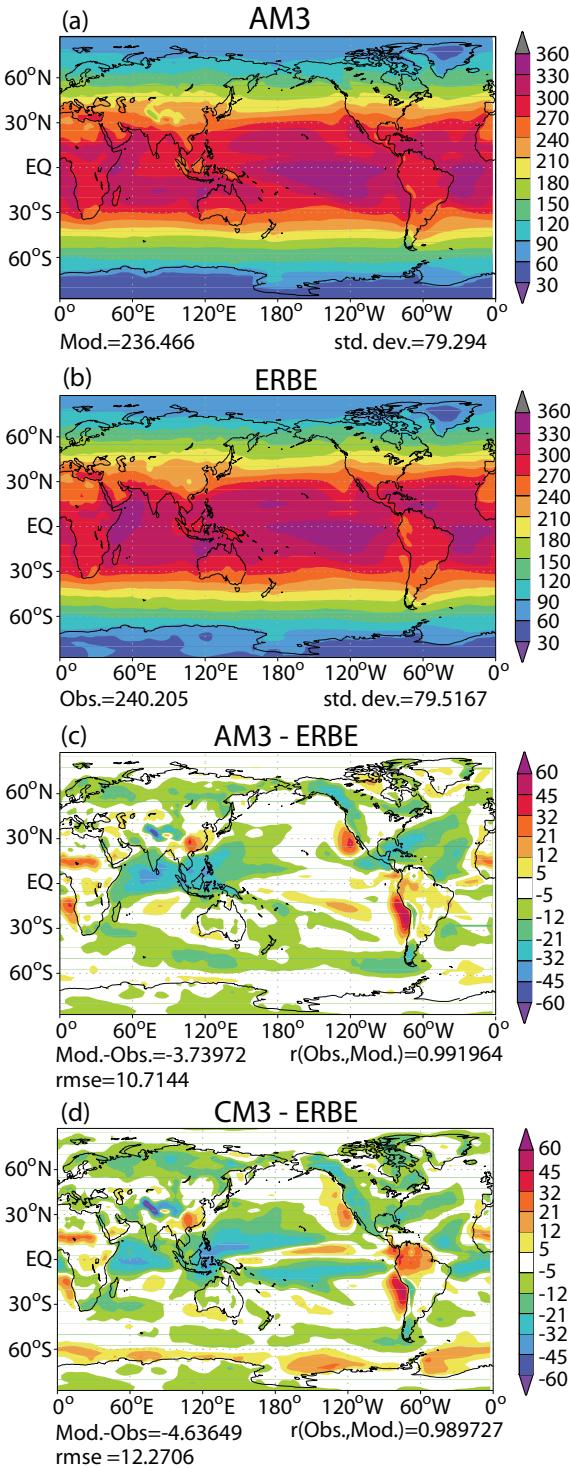


Fig. 10

Outgoing Longwave Radiation (W m^{-2})

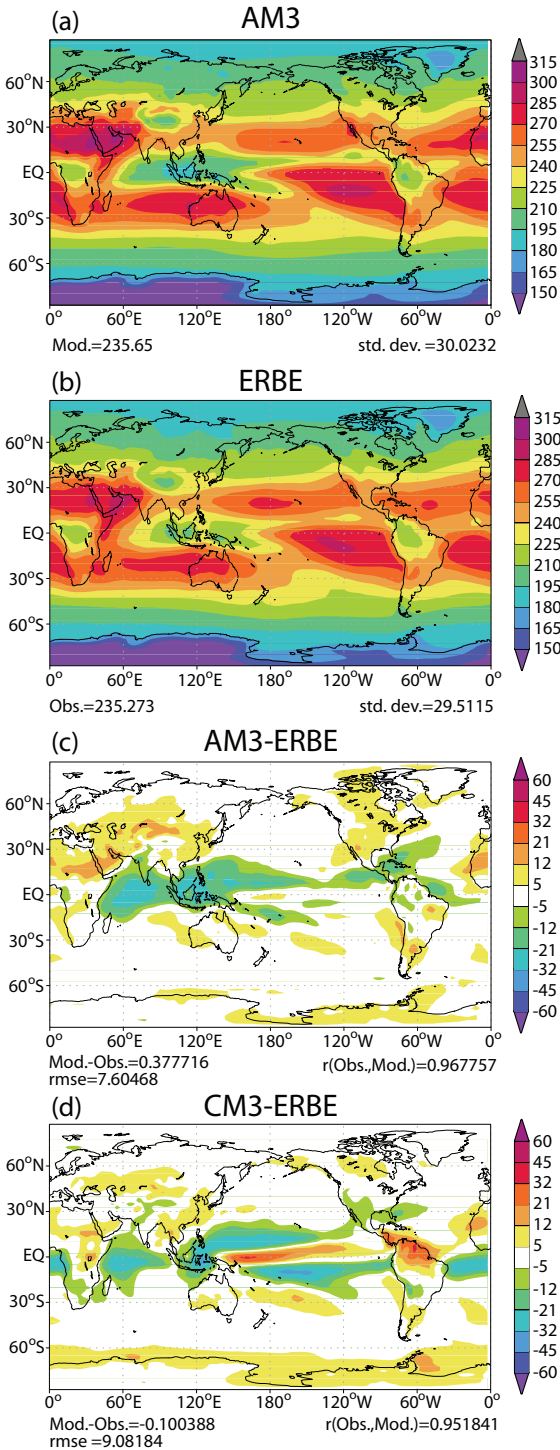
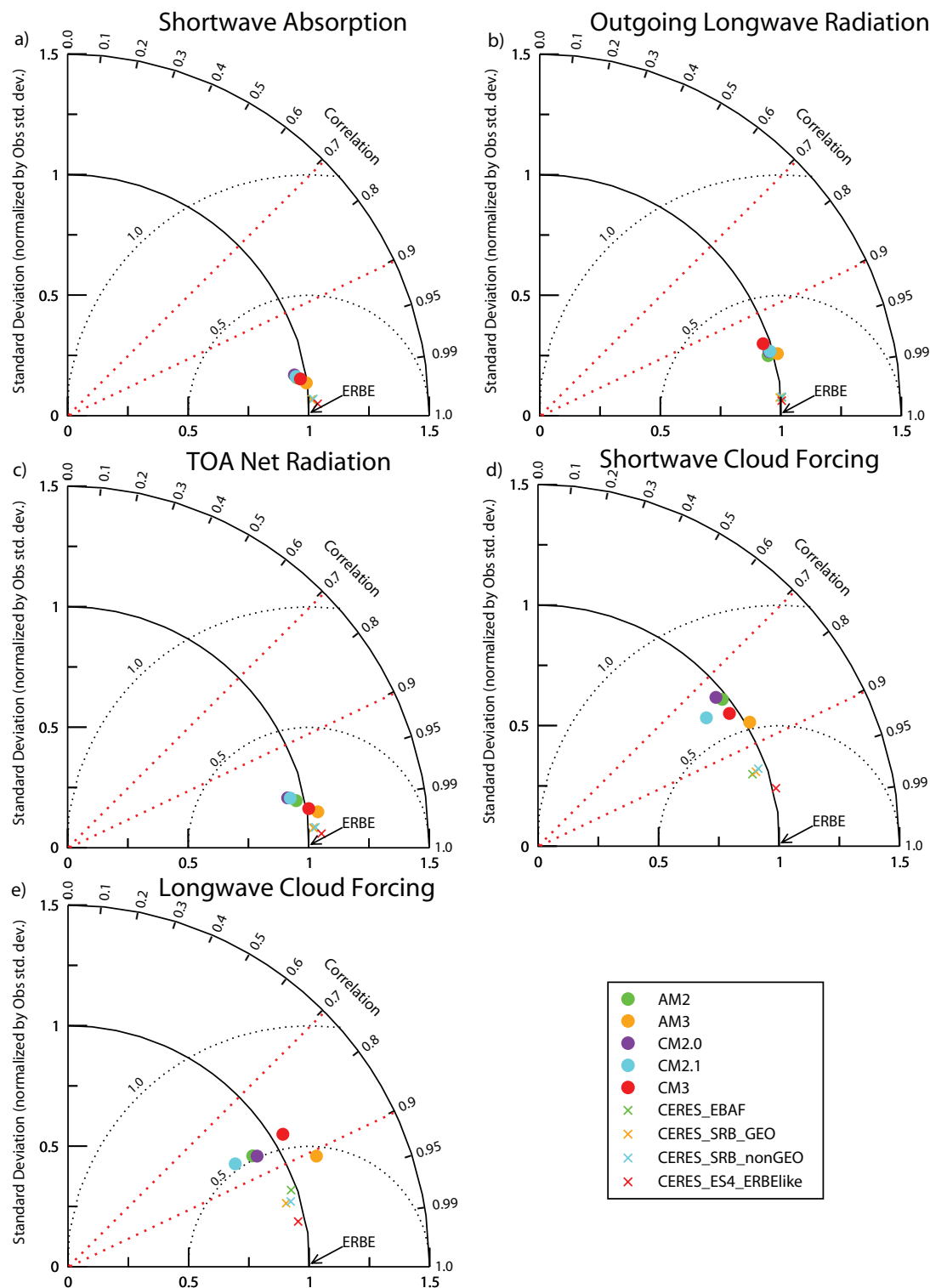


Fig. 11

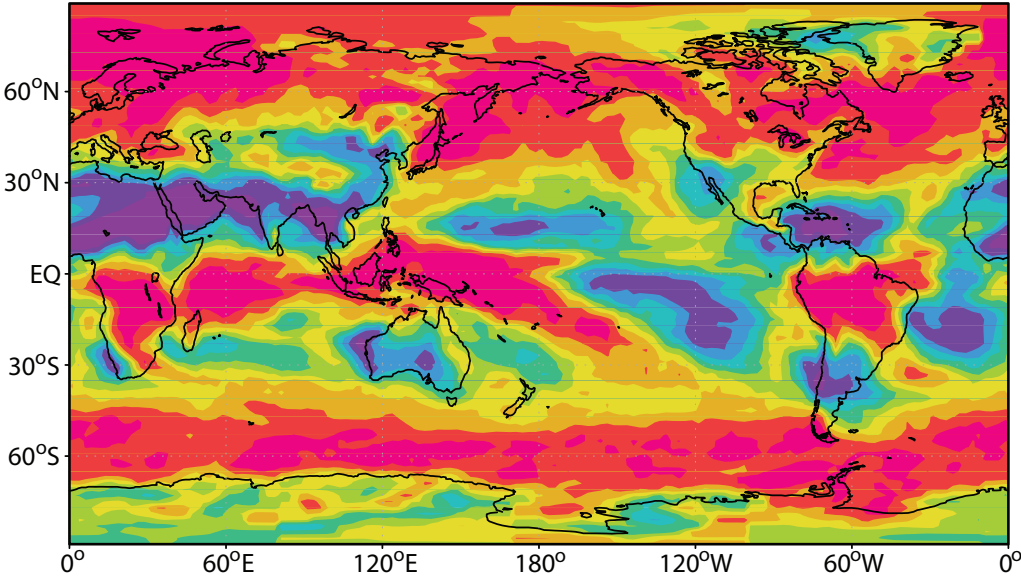


Dotted arcs: RMS error; Solid arcs: standard deviation (both normalized by obs standard deviation)

Fig. 12

Cloud Fraction Jan 2007

(a) AM3 CALIPSO Simulator



(b) CALIPSO

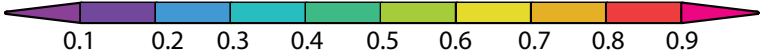
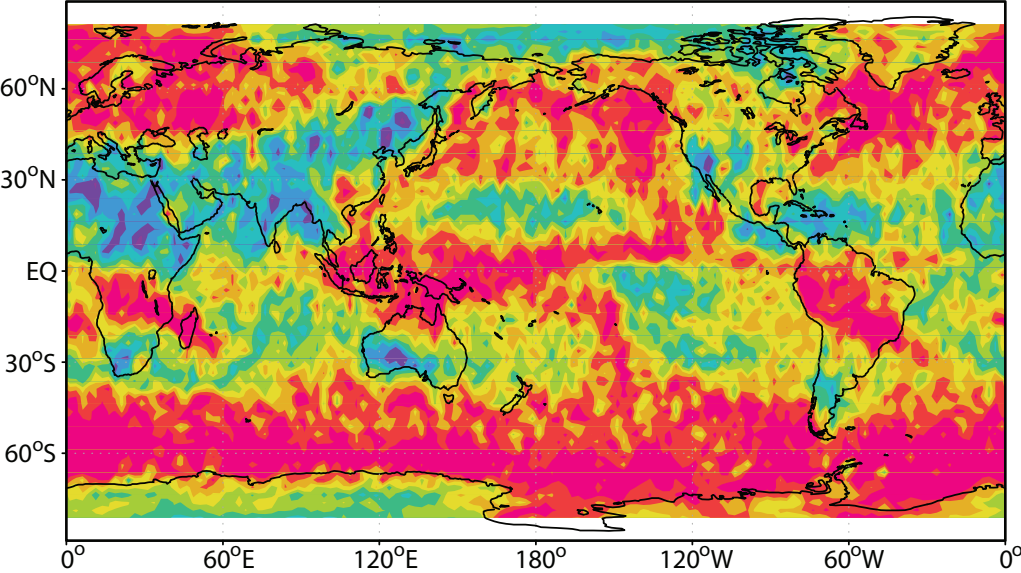


Fig. 13

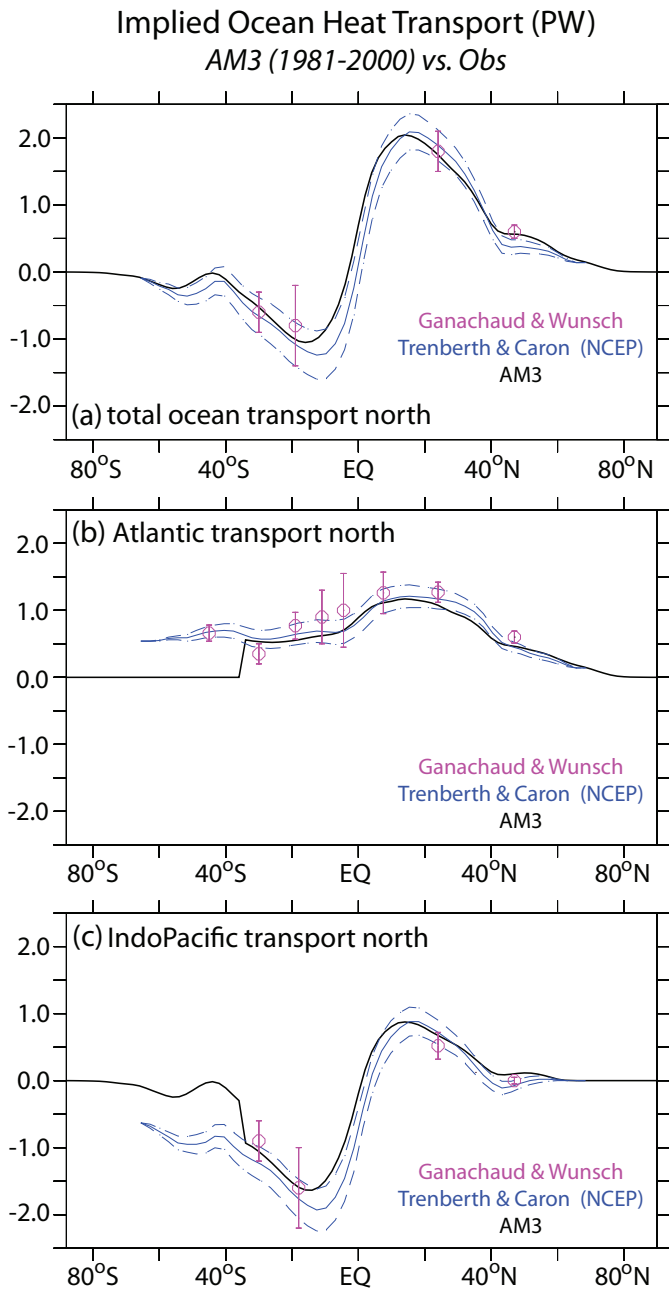


Fig. 14

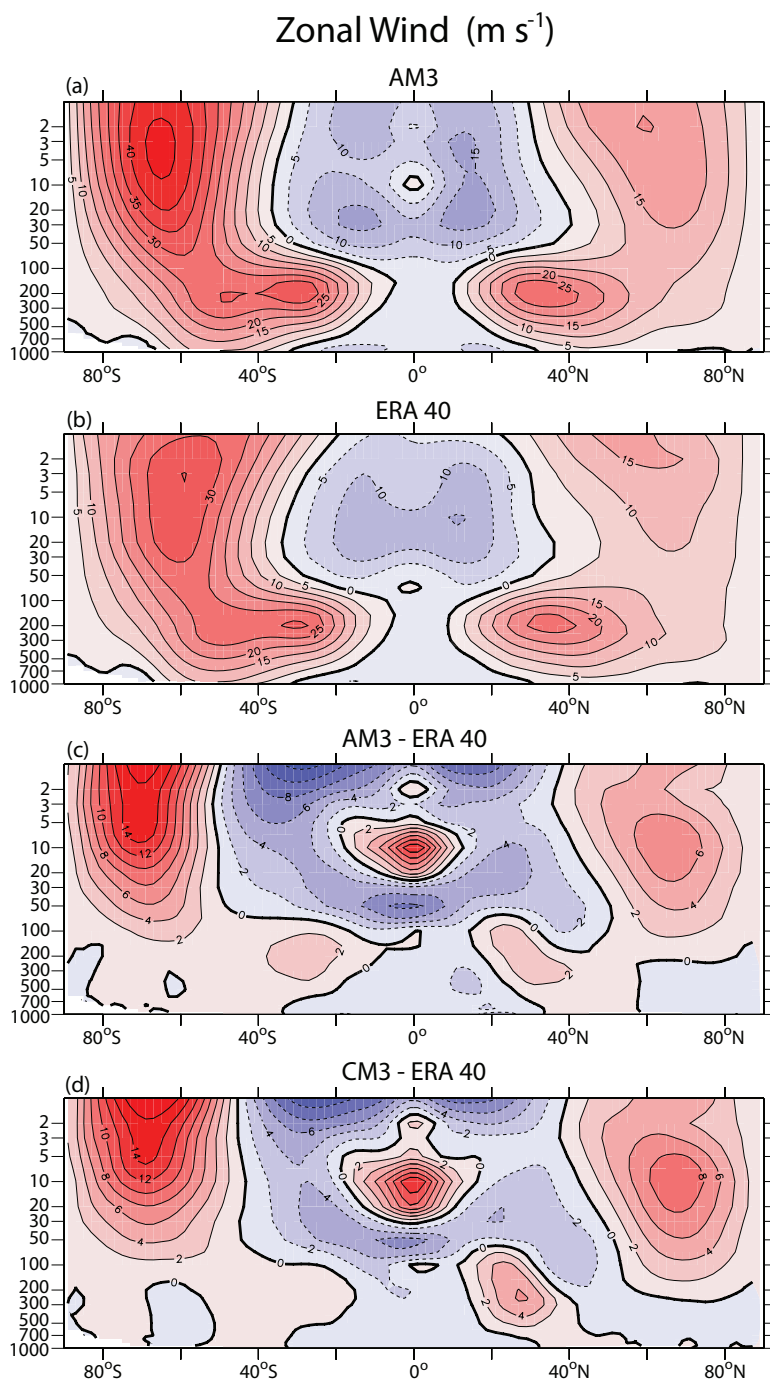


Fig. 15

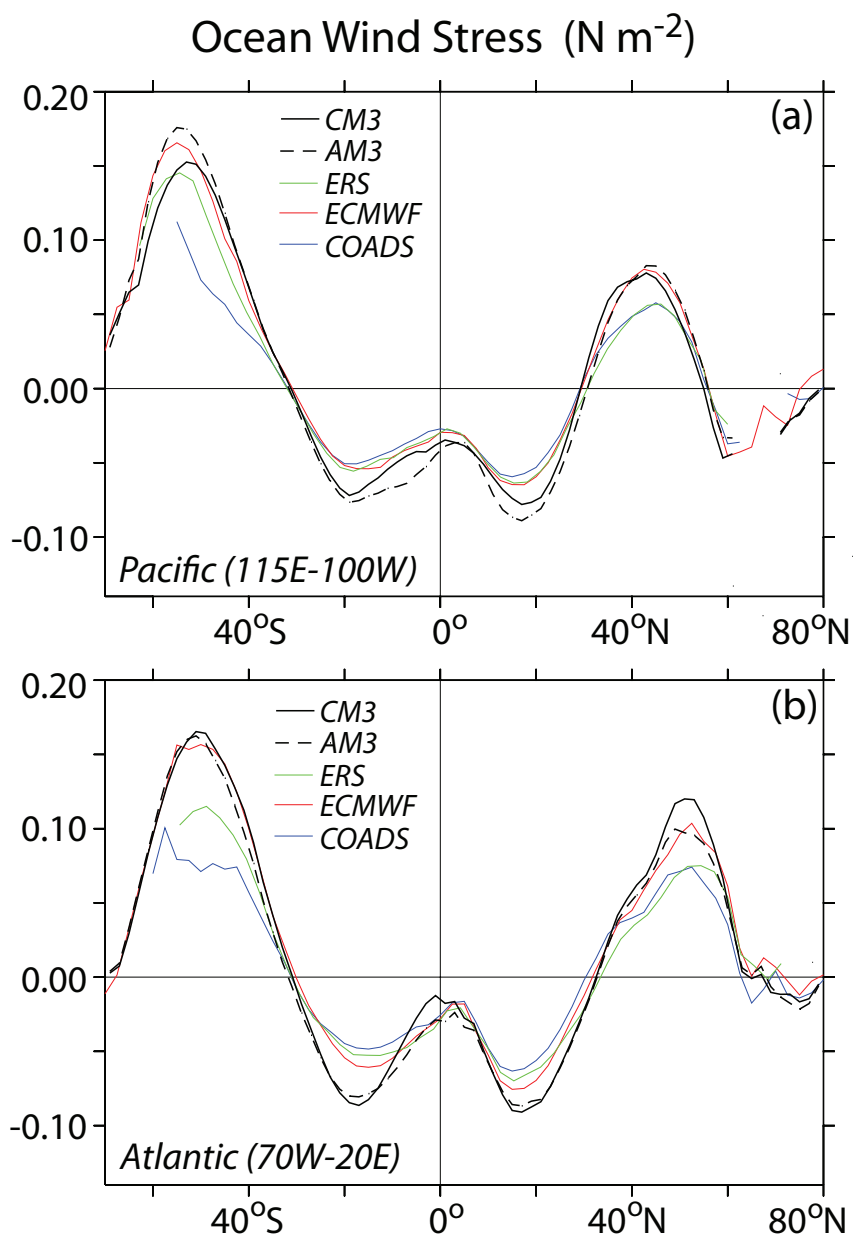


Fig. 16

DJF Northern Hemisphere Sea-Level
Pressure minus 1013.25 hPa (hPa)

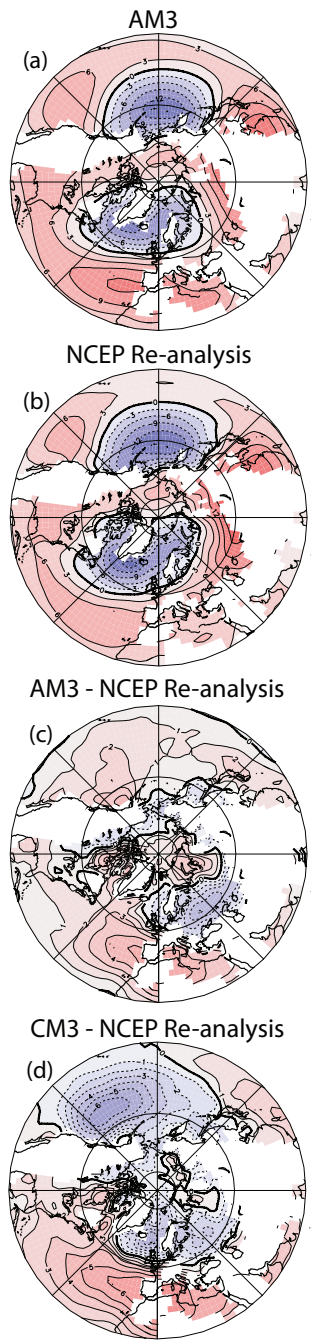


Fig. 17

500 - hPa Zonal Asymmetry (m)

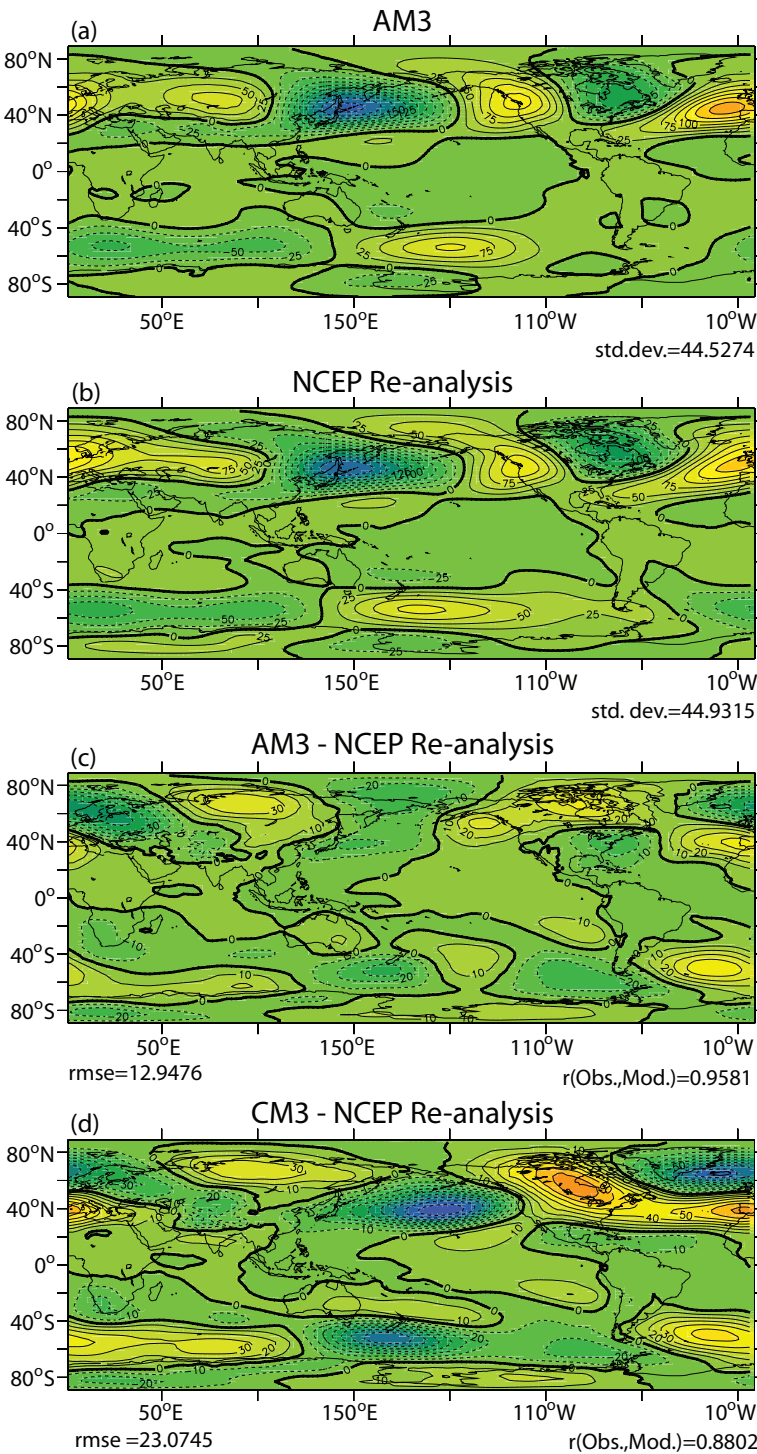


Fig. 18

Regression Coefficient (Precipitation, Nino-3 Index) x S.D. (Nino-3 Index) (mm/day)

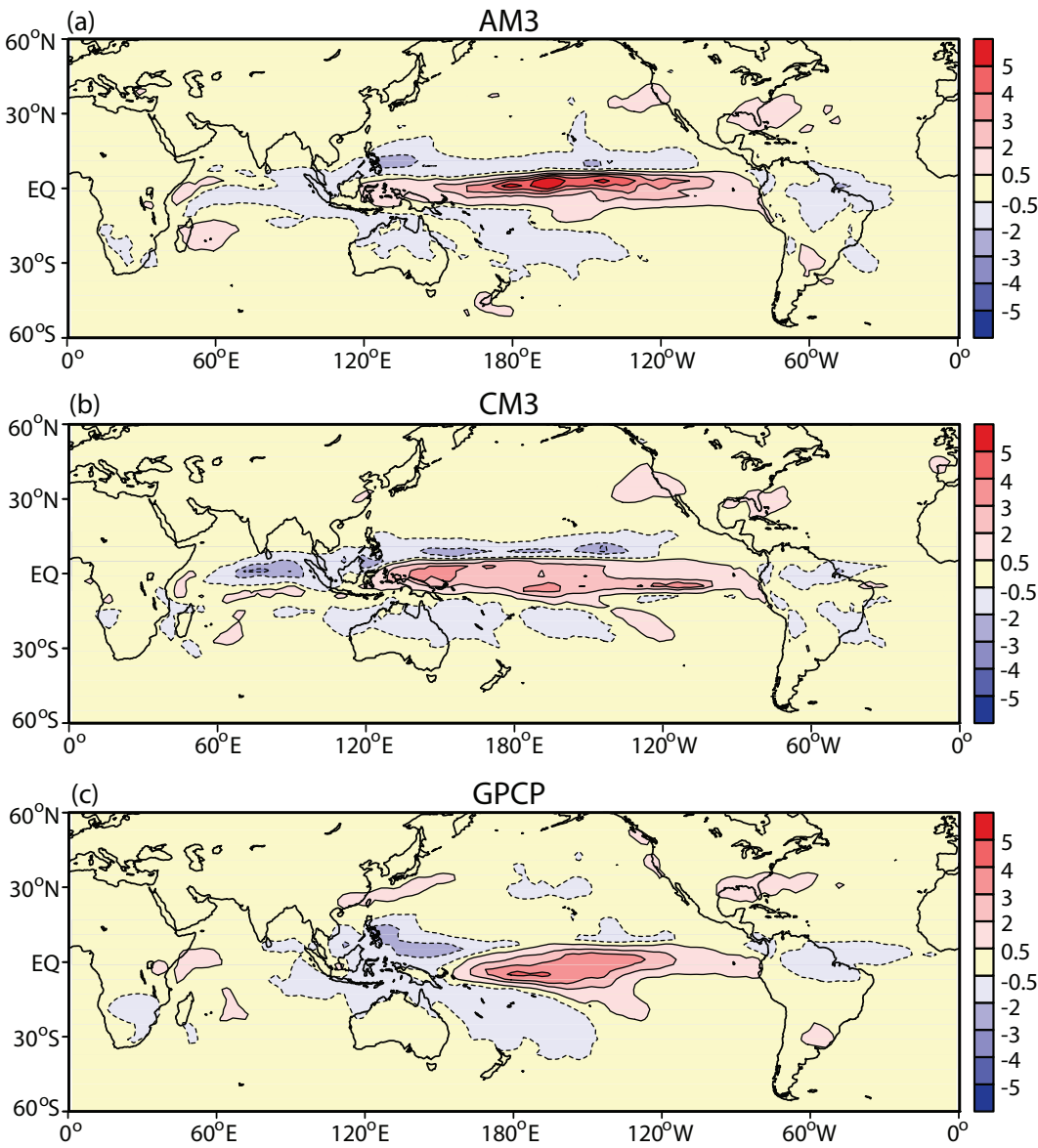
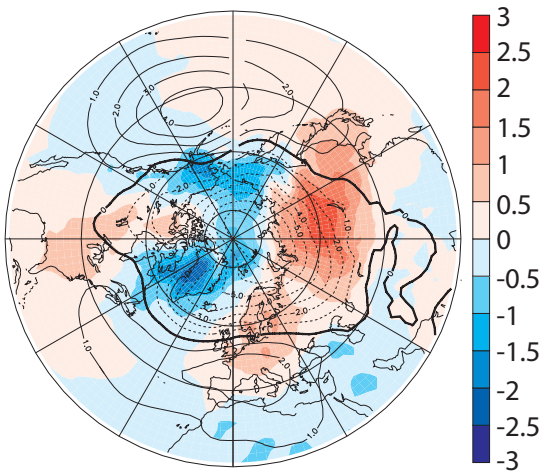


Fig. 19

Northern Annular Mode

(a) AM3



(b) Observations

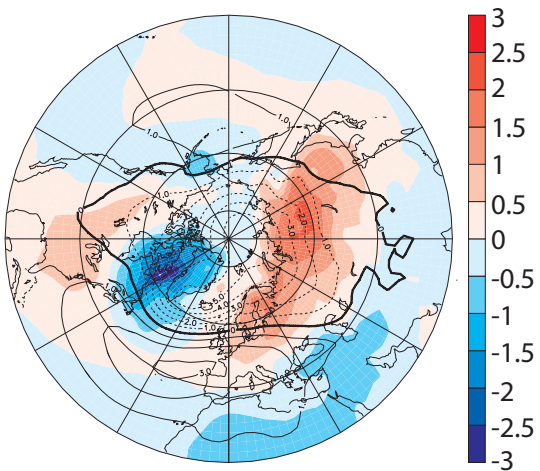
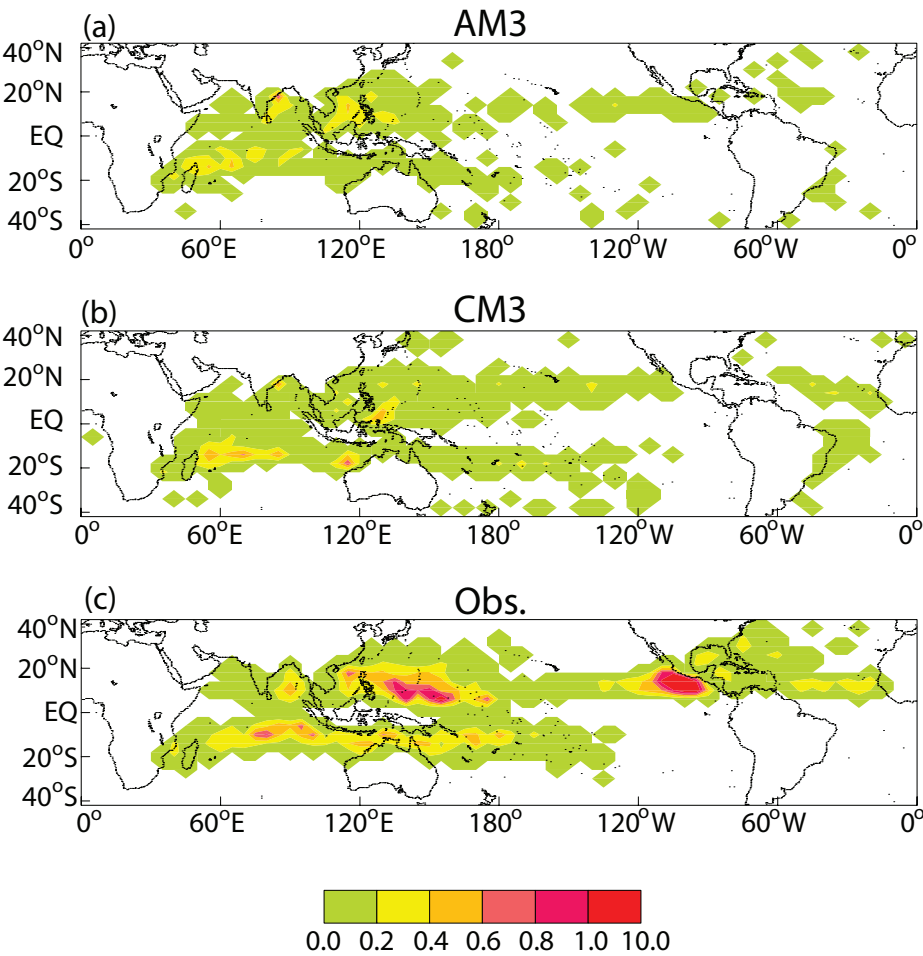


Fig. 20

Tropical-Cyclone Frequency (storms/year)



Tropical-Wave Spectrum

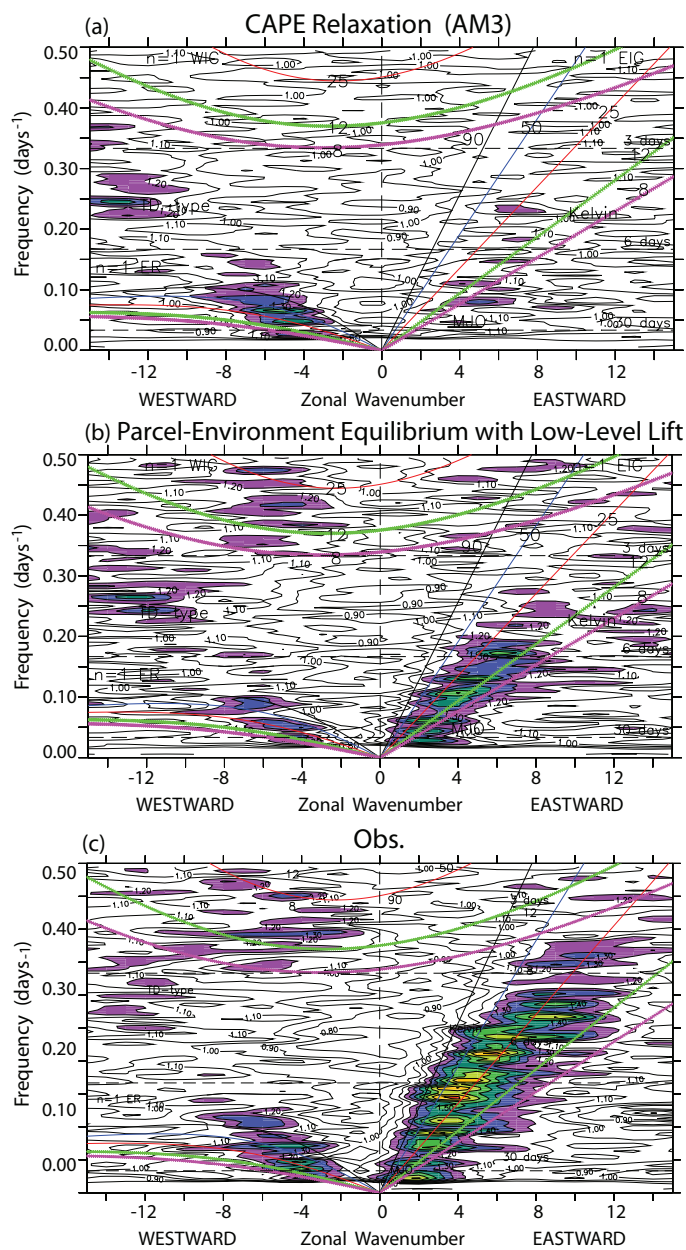


Fig. 22

Temperature ($^{\circ}\text{C}$)

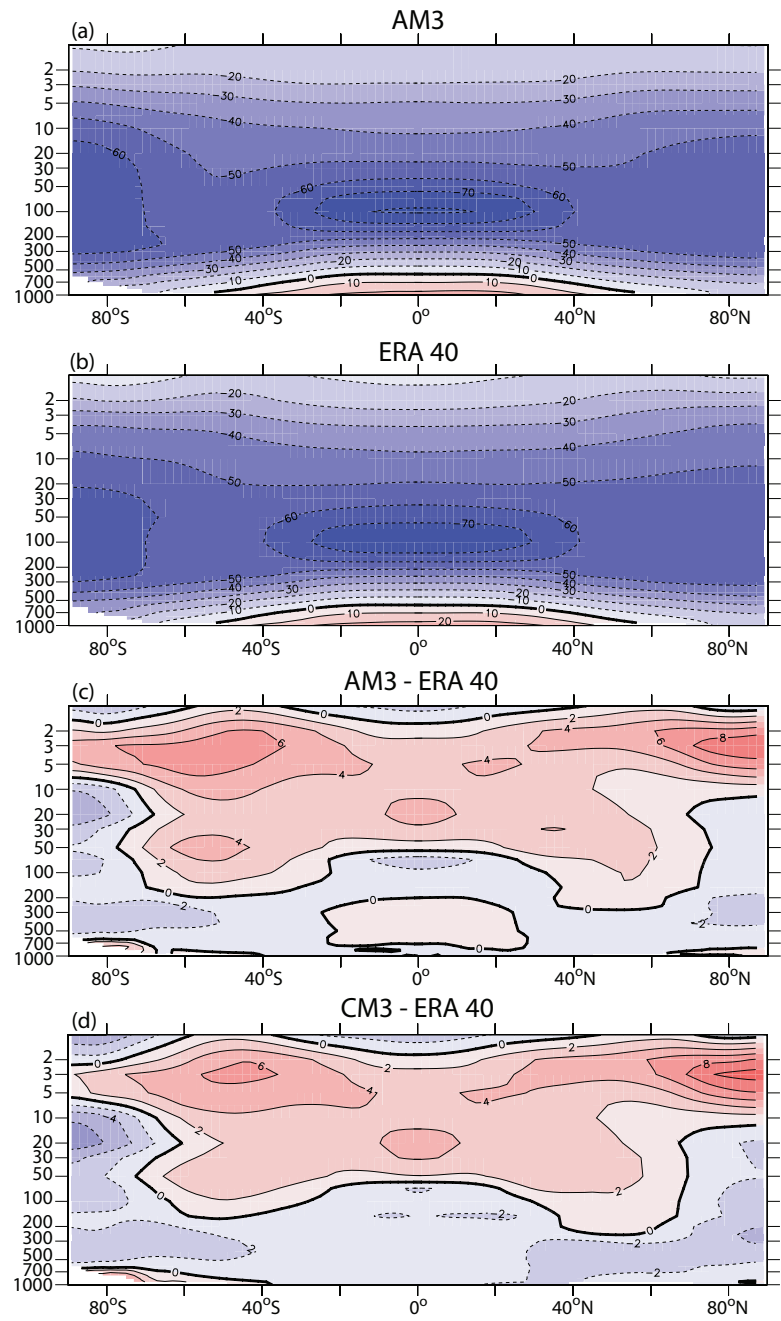


Fig. 23

Sea Surface Temperature ($^{\circ}\text{C}$)

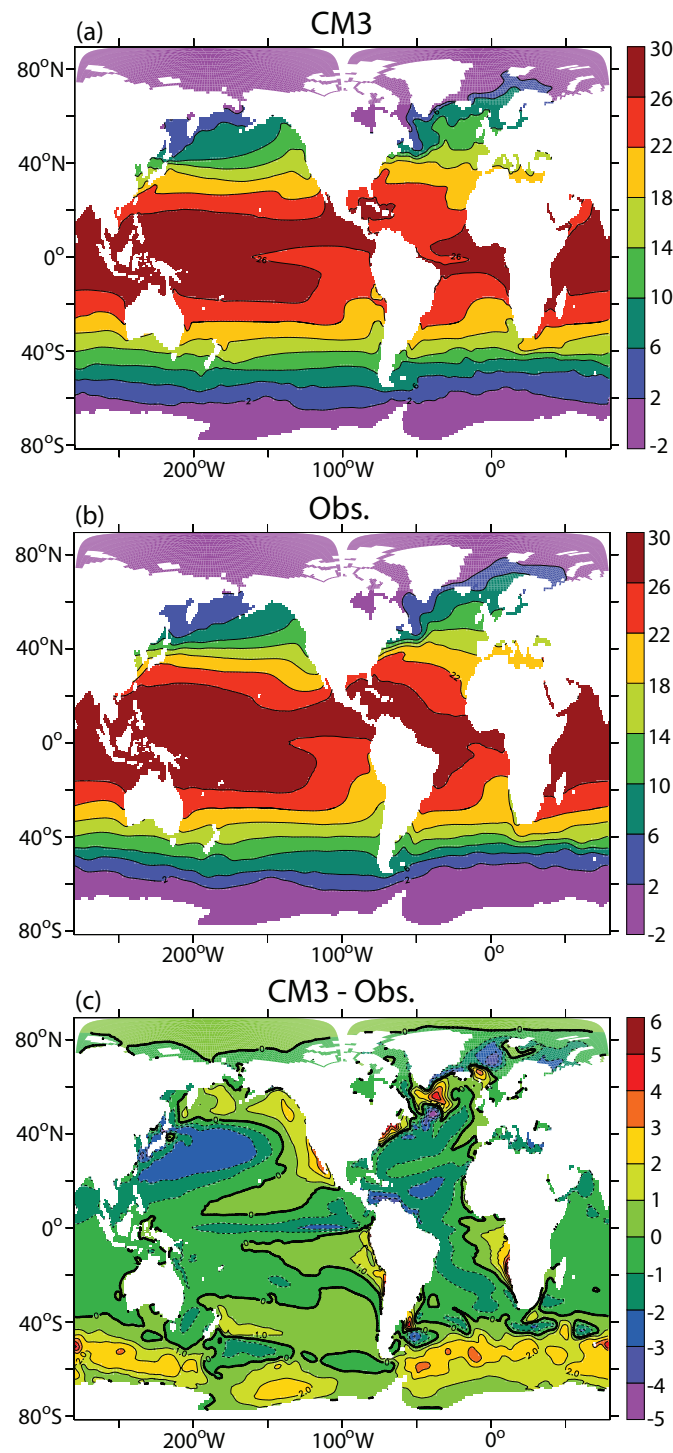


Fig. 24
2-m Temperature (°C)

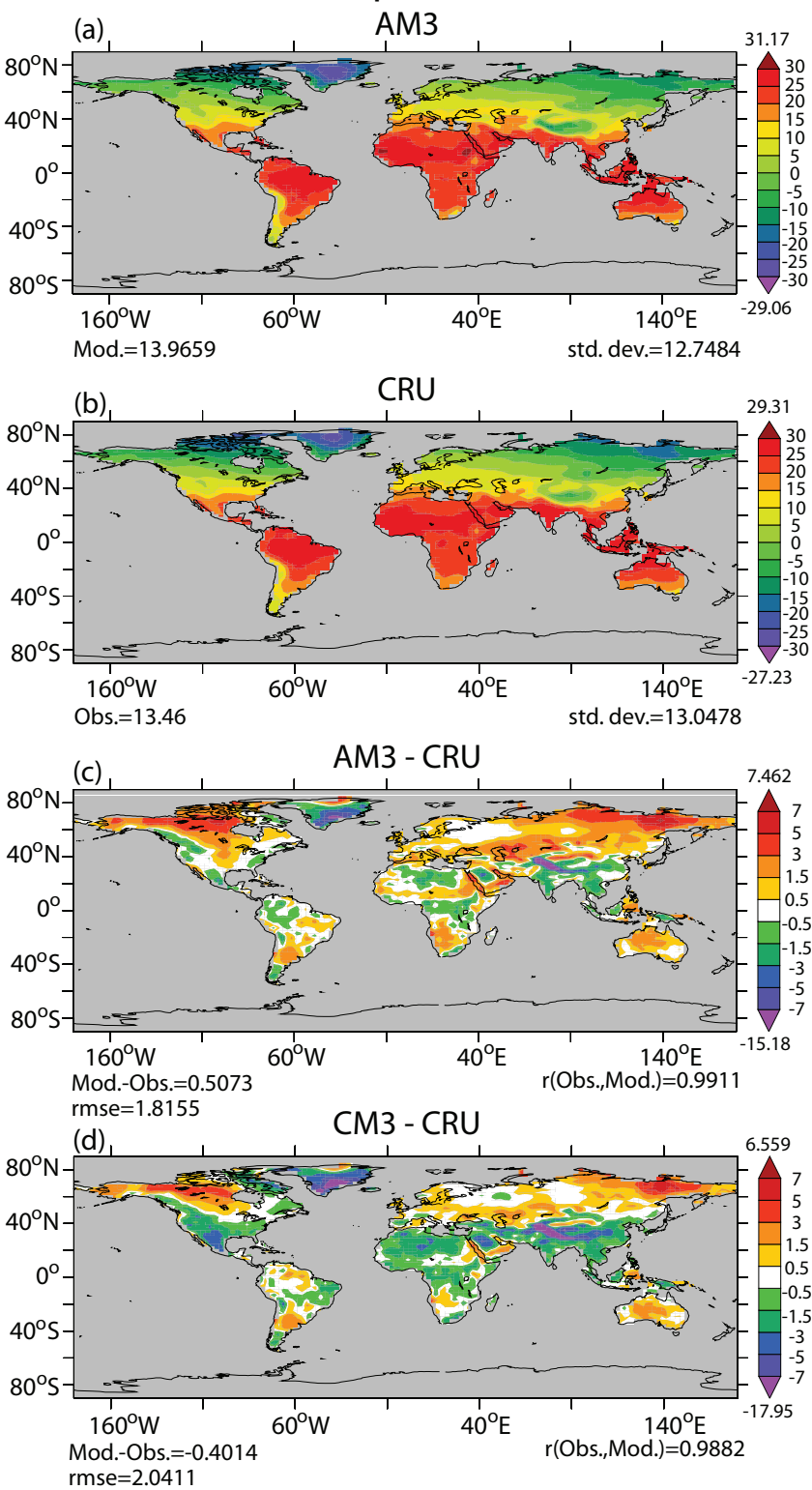


Fig. 25

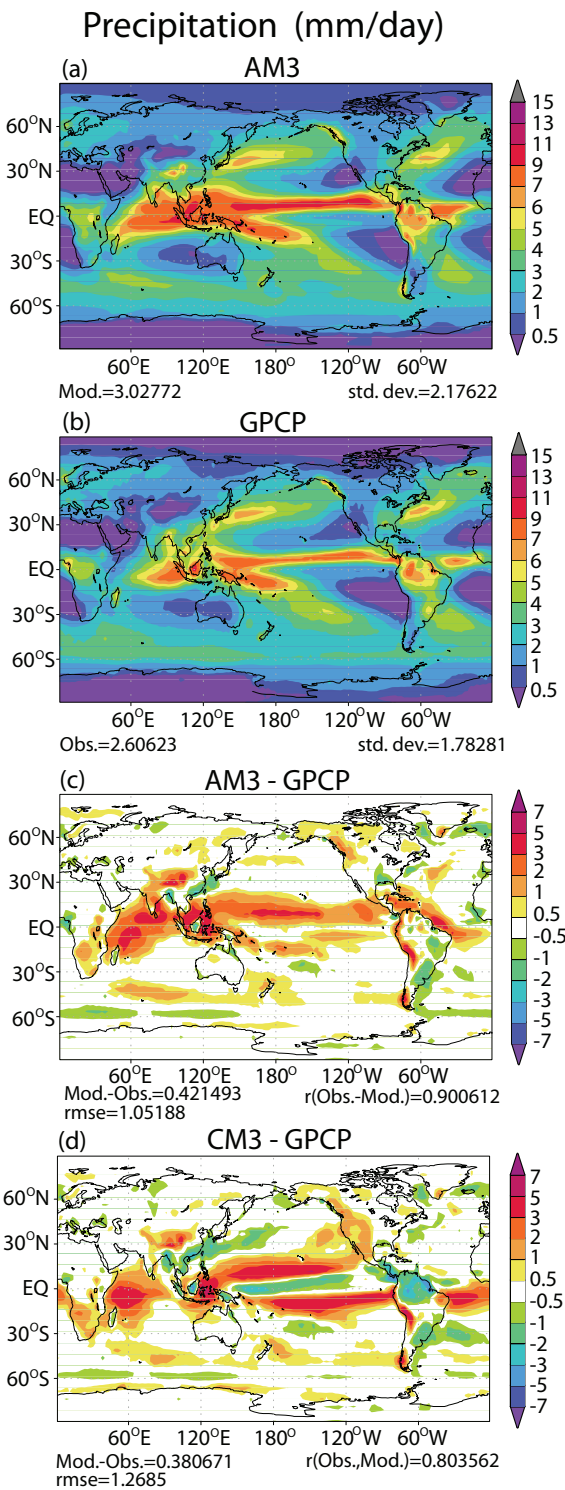


Fig. 26

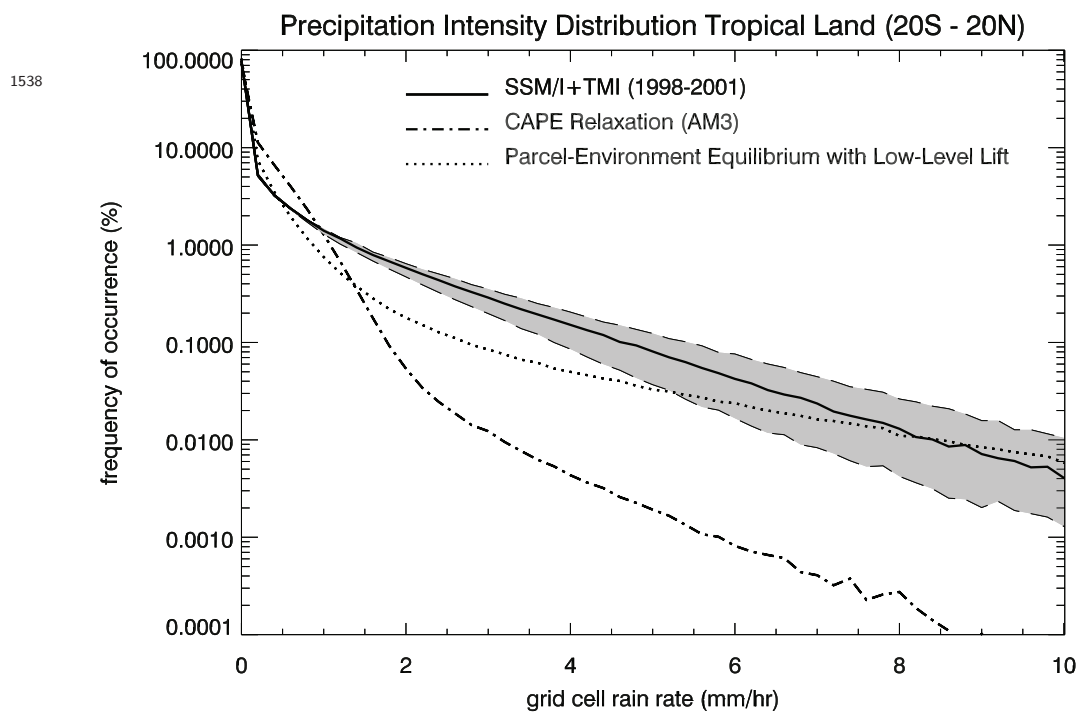


Fig. 27

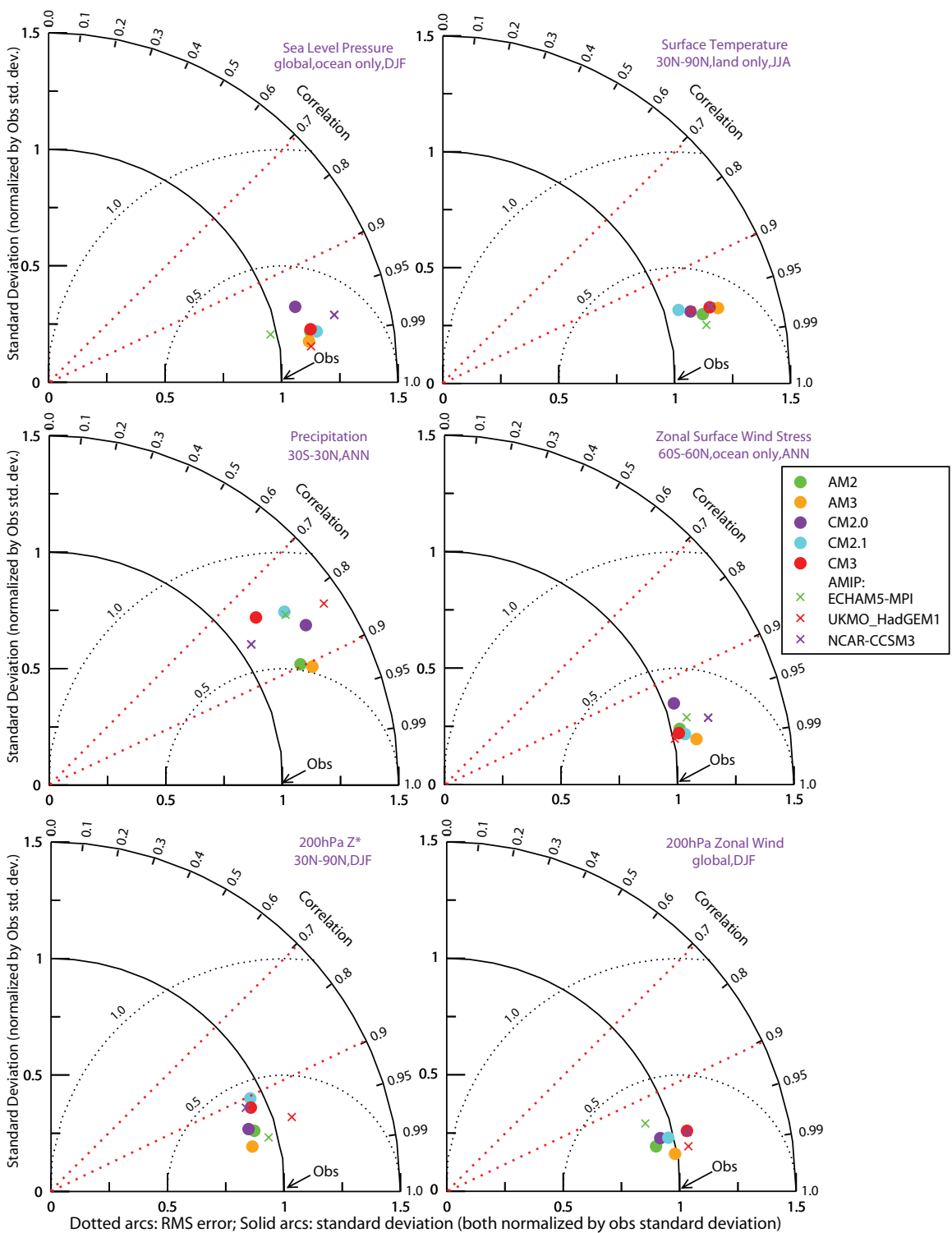


Fig. A1

Annual-Mean Sea-Ice Extent

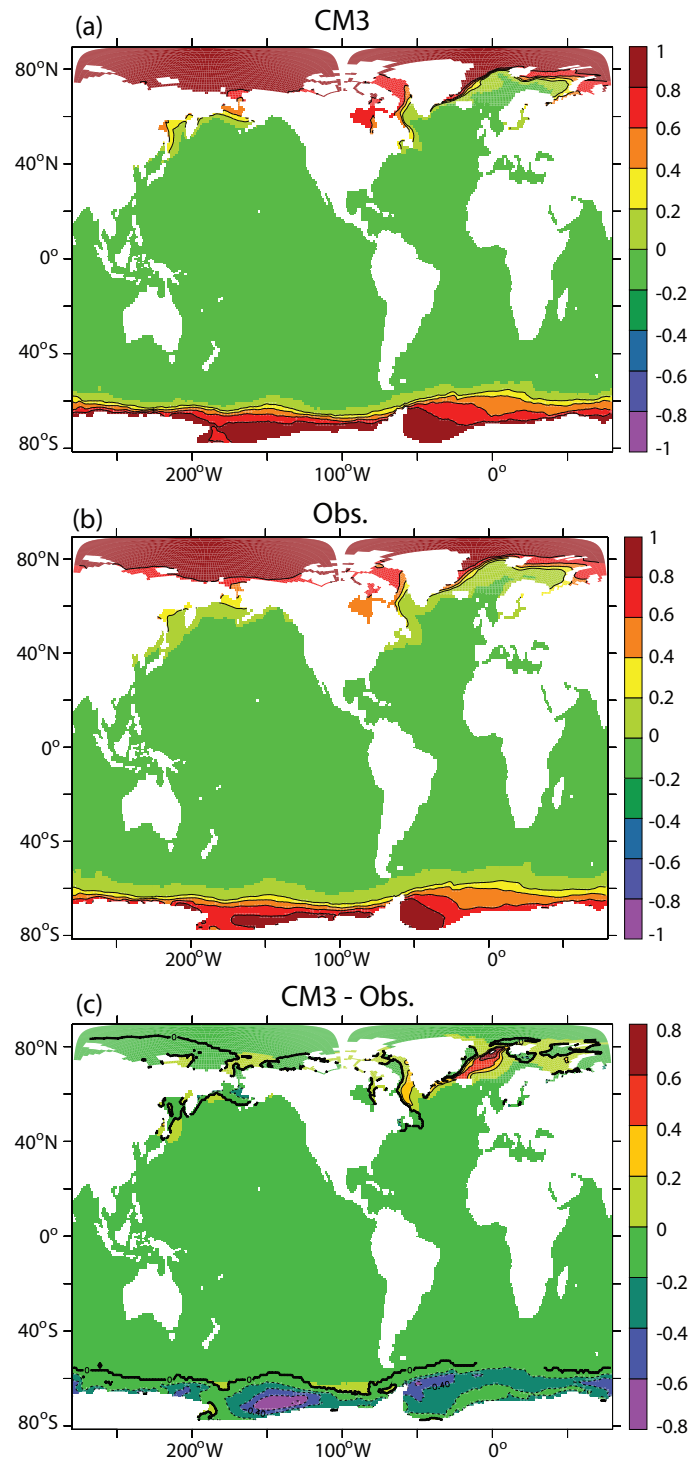


Table 1. Coefficients a_k and b_k for calculation of interface pressures using $p = a_k + b_k \times p_s$, where p is pressure and p_s is surface pressure (Simmons and Burridge, 1981). Pressures and heights of interface levels corresponding to a scale height of 7.5 km and $p_s = 1013.25$ hPa are also shown.

k	a_k (Pa)	b_k	p (hPa)	z (km)
1	1	0	0.01	86.45
2	2.6972	0	0.03	79.00
3	5.1714	0	0.05	74.12
4	8.8946	0	0.09	70.05
5	14.248	0	0.14	66.52
6	22.072	0	0.22	63.24
7	33.613	0	0.34	60.08
8	50.481	0	0.50	57.03
9	74.800	0	0.75	54.08
10	109.40	0	1.09	51.23
11	158.00	0	1.58	48.48
12	225.44	0	2.25	45.81
13	317.90	0	3.18	43.23
14	443.19	0	4.43	40.74
15	611.12	0	6.11	38.33
16	833.74	0	8.34	36.00
17	1125.8	0	11.3	33.75
18	1505.2	0	15.1	31.57
19	1993.2	0	19.9	29.46
20	2614.9	0	26.2	27.43
21	3399.8	0	34.0	25.46
22	4382.1	0	43.8	23.56
23	5600.9	0	56.0	21.72
24	7100.7	0	71.0	19.94
25	8931.8	0	89.3	18.22
26	11150	0	111	16.55
27	13817	0	138	14.94
28	17001	0	170	13.39
29	20776	0	208	11.88
30	23967	0.01253	252	10.43

31	25528	0.04887	305	9.01
32	25671	0.10724	365	7.65
33	24609	0.18455	433	6.37
34	22641	0.27461	505	5.23
35	20147	0.36914	576	4.24
36	17478	0.46103	642	3.42
37	14860	0.54623	702	2.75
38	12415	0.62305	755	2.20
39	10201	0.69099	802	1.75
40	8241.5	0.75016	843	1.38
41	6534.4	0.80110	877	1.08
42	5066.2	0.84453	906	0.84
43	3815.6	0.88127	931	0.63
44	2758.6	0.91217	952	0.47
45	1870.6	0.93803	969	0.33
46	1128.3	0.95958	984	0.22
47	510.48	0.97747	996	0.13
48	0.	0.99223	1005	0.06
49	0.	1	1013	0

1548

1549

Table 2. Global land, area-average of standard deviation of 2-m temperature (1981-2000) (°C)

<i>Season</i>	<i>CRU2.0</i>	<i>CM2.1</i>	<i>CM3</i>
Annual	0.567	0.768	0.677
December-January-February	1.197	1.639	1.391
March-April-May	0.919	1.280	1.178
June-July-August	0.675	1.037	0.878
September-October-November	0.820	1.127	0.925